A Beginner's Guide to Interferometric SAR Concepts and Signal Processing

MARK A. RICHARDS, Senior Member, IEEE
Georgia Institute of Technology

Interferometric synthetic aperture radar (IFSAR, also abbreviated as InSAR) employs pairs of high resolution SAR images to generate high quality terrain elevation maps using phase interferometry methods. IFSAR provides an all-weather, day/night capability to generate measurements of terrain elevation on a dense grid of sample points with accuracies of ones of meters. Both spaceborne and airborne IFSAR systems are in use.

In this paper we present a tutorial introduction to the concepts, techniques, and applications of IFSAR. After a brief introduction to digital elevation models (DEMs) and digital terrain elevation data (DTED), the fundamental IFSAR equation relating interferometric phase measurements to terrain elevation is derived from simple geometric considerations. The central section of the paper describes the major algorithmic steps required to form an IFSAR terrain map. Finally, variations of IFSAR for mapping terrain elevation or reflectivity changes are briefly described. A web site at users.ece.gatech.edu/∼mrichard/AESS_IFSAR.htm provides access to color versions of many of the IFSAR images included in this paper.

Manuscript received April 24, 2005; revised September 11, 2005; released for publication December 1, 2006.

Refereeing of this contribution was handled by P. K. Willett.

Author's address: School of Electrical and Computer Engineering, Georgia Institute of Technology, 244 Ferst Drive, Atlanta, GA 30332-0250, E-mail: (mark.richards@ece.gatech.edu).

I. INTRODUCTION

Interferometric synthetic aperture radar (IFSAR, also abbreviated as InSAR) is a technique for using pairs of high resolution SAR images to generate high quality terrain elevation maps, called digital elevation maps (DEMs), using phase interferometry methods. The high spatial resolution of SAR imagery enables independent measurements of terrain elevation on a dense grid of sample points, while the use of phase-based measurements at microwave frequencies attains height accuracies of ones of meters. Furthermore, the use of active microwave radar as the sensor inherently provides an all-weather, day/night capability to generate DEMs. Variations on the IFSAR concept can also provide high quality measurements of changes in the terrain profile over time, or of changes in the reflectivity of the terrain.

In this paper we present an introductory overview of the concepts, techniques, and applications of IFSAR. First, the fundamental IFSAR relationship for terrain elevation mapping is derived from simple geometric considerations. The central section of the paper describes the major algorithmic steps required to form an IFSAR terrain map. Finally, variations of IFSAR for mapping terrain elevation or reflectivity changes are briefly described.

An excellent first introduction to the concepts and issues in IFSAR is given by Madsen and Zebker in [1]. Detailed tutorial developments of IFSAR with an airborne radar perspective are given in the spotlight SAR textbooks by Jakowatz et al. [2] and Carrara et al. [3]. An analysis from a spaceborne radar perspective is given in the book by Franceschetti and Lanari [4]. The tutorial paper by Rosen et al. [5] also emphasizes spaceborne systems and provides a good overview of space-based IFSAR applications, as well as an extensive bibliography. Bamler and Hartl [6] is another excellent tutorial paper, again with a spaceborne emphasis. Additional tutorial sources are [7] and [8]. Early attempts at interferometric radar are described in [9]–[11]. The first descriptions of the use of coherent (amplitude and phase) imagery for IFSAR were reported in [12]–[14]. The first IFSAR-related patent application was apparently that of D. Richman, then at United Technologies Corp. [15]. The application was filed in 1971 but was placed under a secrecy order, and not granted until 1982 [1].

A variety of technology alternatives exist for generating high accuracy, high resolution terrain maps. In addition to IFSAR, these include at least optical and radar photogrammetry, and laser radar altimeters (LIDAR). Fig. 1 illustrates the approximate relative costs and accuracies of some of these technologies. Comparisons of these technologies are given in [16]–[19]; here, we restrict out attention to IFSAR.

II. DIGITAL TERRAIN MODELS

A digital terrain model (DTM) is a digital representation of the elevation of a portion of the Earth's surface [20]. It typically is comprised of elevation measurements for specified points, lines, and surface elements, and may also include an interpolation scheme for estimating elevation between sample points and descriptive metadata. The term digital elevation model or digital elevation map (DEM) usually implies a simpler array of regularly spaced elevation values referenced to a standard geographic coordinate system [21]. The term DEM also refers to a specific class of data products available from the U.S. Geological Survey (USGS). The data in a DTM or DEM is intended to represent the elevation of the "bare" or "bald" Earth. In contrast, a digital surface model (DSM) is a representation of the top of the terrain rather than the bare Earth. For example, in a forested area the DSM would give the elevation of the tops of the trees, while the DEM would describe the elevation of the forest floor.

DTMs have an expanding variety of uses. The most obvious and important is topographic mapping, which in turn is useful for such diverse applications as three-dimensional visualization, terrain analysis for "precision agriculture," line-of-sight (LOS) mapping for telecommunications tower siting and utilities routing, disaster analysis (e.g. flood mapping), navigation, and so forth [22]. A less obvious example is the use of DTMs to enhance radar ground moving target indication (GMTI) and space-time adaptive processing (STAP) performance by incorporating knowledge of the terrain into the clutter statistics estimation procedures at the core of GMTI and STAP algorithms [23].

What degree of accuracy makes for a useful DEM? The quality of a DEM is determined by the spacing of the grid points (the denser the grid, the better) and the accuracy of the individual elevation values. A particular DEM standard is the digital terrain elevation data (DTED) specification[1] developed by the U.S. National Geospatial Intelligence Agency (NGA) and its predecessors [24]. The DTED specification classifies DEM data into 6 "DTED levels" numbered 0 through 5. Table I shows the increasing level of detail associated with increasing DTED levels [24–26]. The Shuttle Radar Topography Mission (SRTM) conducted in 2000 collected data from low Earth orbit intended to support mapping of 80% of the Earth's surface at DTED level 2 [27, 28]. The U.S. Army's "rapid terrain visualization" (RTV) demonstration developed an airborne system for near real-time generation of DTED level 3 and 4 products over localized areas [25]; an example image is given in Section VIB4. DTED level 5 data typically requires use of an airborne LIDAR system. Fig. 2 compares a small portion of a DEM of the same area rendered at DTED level 2 derived from SRTM data (Fig. 2(a)) and at DTED level 3, derived from E-SAR data (Fig. 2(b)).[2]

IFSAR images typically rely on pseudocolor mappings to make the height detail more perceptible. It is difficult to appreciate the information in Fig. 2 and other IFSAR images in this paper when they are printed in grayscale. Selected images from this paper are available in color at users.ece.gatech.edu/∼mrichard/AESS_IFSAR.htm.

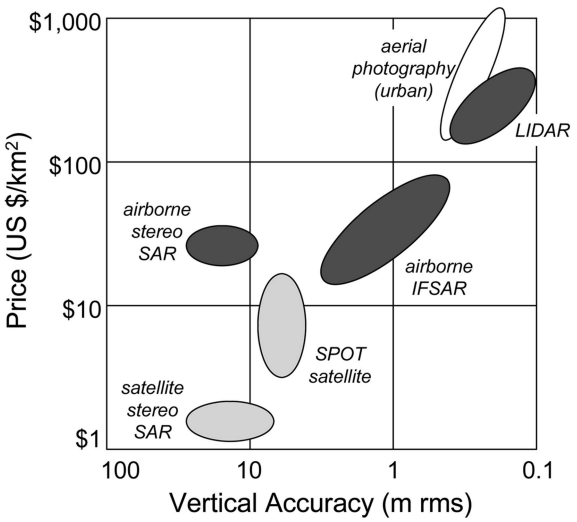

Fig. 1. Relative cost and accuracy of DEM generation technologies. (After Mercer [19].)

TABLE I
Selected DTED Specifications

DTED Level	Post Spacing	Absolute Vertical Accuracy	Relative Vertical Accuracy
0	30.0 arc sec ∼1000 m	not specified	not specified
1	3.0 arc sec ∼100 m	30 m	20 m
2	1.0 arc sec ∼30 m	18 m	12–15 m
3†	0.3333 arc sec ∼10 m	10† m	1–3† m
4†	0.1111 arc sec ∼3 m	5† m	0.8† m
5†	0.0370 arc sec ∼1 m	5† m	0.33† m

†Accuracies for DTED levels 3–5 are proposed, but not final and not included in MIL-PRF-89020B. Various sources report varying values for the proposed accuracy.

[1]An updated version of the DTED specification, called "high resolution terrain information" (HRTI), is under development as standard MIL-PRF-89048.

[2]E-SAR is the "experimental SAR" developed by the German Aerospace Center (DLR). See www.op.dlr.de/ne-hf/projects/ESAR/esar_englisch.html.

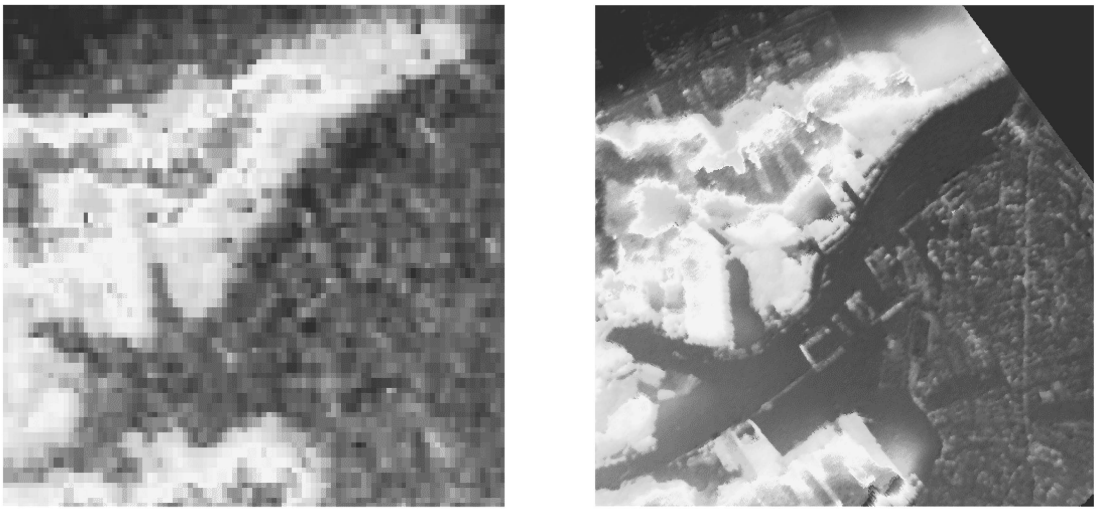

(a) (b)

Fig. 2. Comparison of two DEMs of a 2 by 2 km area of Eichenau (close to Munich, Germany) derived from different DTED data levels. (a) Derived from DTED level 2 SRTM data. (b) Derived from DTED level 3 E-SAR data. (Images courtesy of German Aerospace Center (DLR), Microwaves and Radar Institute. Used with permission.)

III. MEASURING TERRAIN HEIGHT

A general stereo imaging geometry is shown in Fig. 3. Two SAR receivers at an elevation H are separated by a baseline B oriented at an angle β with respect to local horizontal. The ranges R and $R + \Delta R$ to a scatterer P at height $z = h$ and ground range y_1 are measured independently at the two receive apertures. The law of cosines gives

$$(R + \Delta R)^2 = R^2 + B^2 - 2BR\cos(\psi + \beta). \tag{1}$$

Equation (1) is solved for the depression angle ψ to the scatterer, and the scatterer height is then obtained easily as

$$h = H - R\sin\psi. \tag{2}$$

A relationship between a change in the scatterer height δh and the resulting change in the difference in range to the two phase receivers $\delta(\Delta R)$, is derived as follows [4]. The desired differential can be broken into two steps:

$$\frac{dh}{d(\Delta R)} = \frac{dh}{d\psi}\cdot\frac{d\psi}{d(\Delta R)} = \frac{dh}{d\psi}\cdot\frac{1}{d(\Delta R)/d\psi}. \tag{3}$$

From (2), $dh/d\psi = -R\cos\psi$. Assuming $R \gg B$ and $R \gg \Delta R$, (1) becomes

$$\Delta R \approx -B\cos(\psi + \beta) \tag{4}$$

so that $d(\Delta R)/d\psi \approx B\sin(\psi + \beta)$. Combining these results gives

$$\frac{dh}{d(\Delta R)} \approx \frac{-R\cos\psi}{B\sin(\psi+\beta)} \quad \Rightarrow$$
$$|\delta h| \approx \frac{\cos\psi}{\sin(\psi+\beta)}\left(\frac{R}{B}\right)|\delta(\Delta R)|. \tag{5}$$

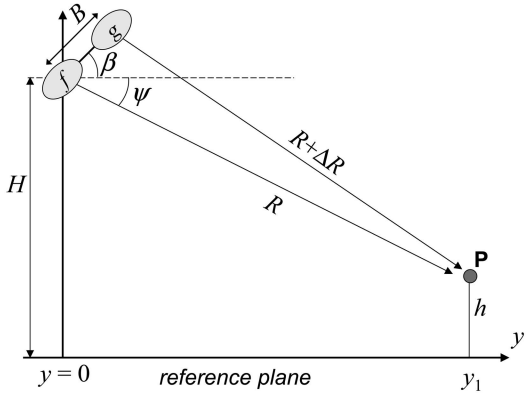

Fig. 3. Stereo imaging geometry.

Equation (5) shows that the error in the height measurement is proportional to the error in the range difference ΔR multiplied by a factor on the order of the ratio (R/B).

Evidently, achieving good height accuracy from significant stand-off ranges requires a large baseline, great precision in measuring ΔR, or both. Optical stereo imaging systems, with their very fine resolution, can achieve good results with a stereo camera pair on a small baseline in one-pass operation (see Section IVA). Conventional SAR-based stereo imaging systems must generally use two-pass operation with significant separation between the two tracks so as to obtain look angle differences from the two tracks to the terrain area of interest on the order of 10° to 20° [29]. However, for IFSAR such large baselines are not practical.

For spaceborne IFSAR systems, the baseline is typically on the order of 100 m, though it can be as large as 1 or 2 km, while the altitude ranges from approximately 250 km (for the space shuttle) to

800 km (for low Earth orbit satellites), giving (R/B) on the order of 2500 to 7000. For airborne systems, the stand-off range is usually on the order of 10 to 20 km, but the baseline is typically only on the order of a few meters to a foot, so that again (R/B) is on the order of several thousand. Because of this large multiplier, it is necessary to have very small values of $\delta(\Delta R)$ if height errors are to be acceptable. Thus, we need to be able to measure small differences in range from the scatterer to the two receive apertures.

As an example, consider the DTED level 2 vertical accuracy requirement of 18 m. Assume for simplicity that $\beta = \psi = 45°$. The SRTM mission operated at an altitude of about 240 km; thus $R \approx 240{,}000/\sin(45°) = 340$ km. The baseline was $B =$ 60 m. To meet the 18 m accuracy requirement would require that the range difference be accurate to within 4.5 mm! Even with subpixel range tracking to 1/20th of a pixel, this is much finer that can be supported by SAR range resolutions. For instance, 1/20th of the SRTM range resolution of 15 m is 0.75 m, bigger than the desired 4.5 mm by a factor of 167.

The need for very fine range differential measurements to achieve usable height accuracies leads to the use of phase instead of time delay in radar interferometry. Phase measurements allow range precisions of fractions of an RF wavelength, and thus enable much better height accuracy. The disadvantage is that phase-based measurements are highly ambiguous. This problem is dealt with in Section VIB.

IV. IFSAR OPERATIONAL CONSIDERATIONS

A. One-Pass versus Two-Pass Operation

IFSAR data collection operations can be characterized as one-pass or two-pass. Fig. 4 illustrates these two cases. In one-pass processing, a platform with two physical receive apertures, each with an independent coherent receiver, collects all of the radar data needed in a single pass by a scenario of interest. The two SAR images $f(x,y)$ and $g(x,y)$ are formed from the two receiver outputs. In two-pass operation, the platform requires only a conventional radar with a single receiver, but makes two flights past the area of interest. The two flight paths must be carefully aligned to establish the desired baseline. The advantages of one-pass operation are the relative ease of motion compensation and baseline maintenance, since the two apertures are physically coupled, and the absence of any temporal decorrelation of the scene between the two images. The major disadvantage is the cost and complexity of the multi-receiver sensor. Conversely, the major advantage of two-pass operation is the ability to use a conventional single-receiver SAR sensor, while the major disadvantage is the difficulty of controlling

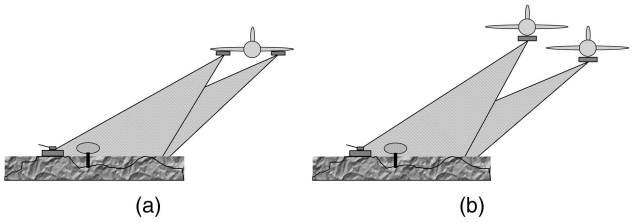

Fig. 4. IFSAR data collection modes. (a) One-pass. (b) Two-pass.

the two passes and compensating the data from the two receivers to carefully aligned collection paths, as well as the possibility of temporal decorrelation of the scene between passes. Because of the motion compensation issue, two-pass operation is more easily applied to spaceborne systems, where the two passes are implemented as either two orbits of the same spacecraft, or with two spacecraft, one trailing the other. In either case, the lack of atmospheric turbulence and the stable and well-known orbital paths make it easier to produce an appropriate pair of IFSAR images. On the other hand, if different orbits of one satellite are used to establish the baseline, suitable orbits can easily be at least a day apart. For example, the RADARSAT system uses orbits 24 days apart to form interferometric images [29]. In such systems, temporal decorrelation may be a significant limiting factor.

B. Spaceborne versus Airborne IFSAR [5]

IFSAR maps can be generated from both satellite and airborne platforms. Satellite systems such as SRTM and RADARSAT provide moderate post (height sample) spacing, typically 30 to 100 m. Vertical accuracies are on the order of 5 to 50 m. Airborne systems generally generate higher resolution SAR maps, which in turn support closer post spacing and higher accuracy; airborne systems routinely provide vertical accuracies of 1 to 5 m on a post spacing of 3 to 10 m. While achievable SAR resolution is independent of range in principle, practical considerations such as the decrease in signal-to-noise ratio (SNR) and the increase in required aperture time with increasing range favor shorter ranges for very high resolution SAR. Airborne LIDAR systems provide the highest quality data, with post spacing of 0.5 to 2 m and vertical accuracy on the order of tens of centimeters [17, 19].

Satellite systems provide nearly global coverage at relatively low cost (see Fig. 1). Their responsiveness and availability depends strongly on when an orbit will provide coverage of the desired region. Numerous concepts have been proposed for satellite constellations that would provide more continuous and rapid global IFSAR coverage, but none are yet fielded. Airborne IFSAR lacks global coverage

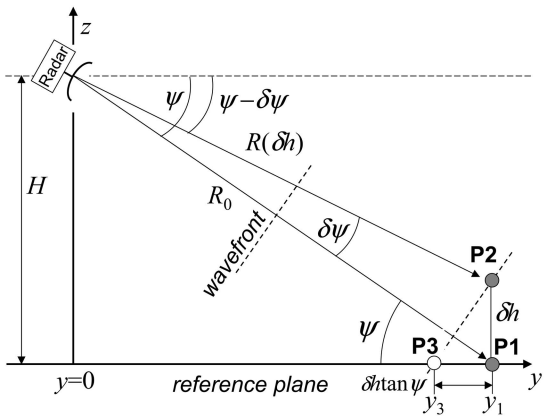

Fig. 5. Geometry for determining the effect of scatterer height on received phase.

capability and has a higher cost per unit area, thus being most useful for localized mapping. Timely access to a given region can be limited by airspace restrictions or simply the time required to transport an instrument to the area. The much lower altitude of airborne systems makes the area coverage rate much smaller as well.

Airborne systems require high precision motion compensation to overcome the defocusing and mislocation effects resulting from path deviations caused by vibration, atmospheric turbulence, and winds. These effects are much reduced or absent in spaceborne systems, although platform orbit and attitude must still be carefully controlled. Spaceborne systems are subject to dispersive ionospheric propagation effects, principally variable path delays in two-pass systems up to tens of meters, that are absent in airborne systems [5]. Both air- and spaceborne systems suffer potential errors due to differential delay through the wet troposphere. For example, using 1995 Shuttle Imaging Radar-C (SIR-C) repeat-track data (not the SRTM mission of 2000), Goldstein [30] estimates rms path length variations of 0.24 cm at both L and C band. For the baselines used in those experiments, this translates into a 6.7 m rms elevation estimate error.

V. BASIC INTERFEROMETRIC SAR RELATIONSHIPS

A. The Effect of Height on the Phase of a Radar Echo

Since IFSAR is based on phase measurements, we begin our derivation of basic IFSAR equations by considering the phase of a single sample of the echo of a simple radar pulse from a single point scatterer. Consider the geometry shown in Fig. 5, which shows a radar with its antenna phase center located at ground range coordinate $y = 0$ and an altitude $z = H$ meters above a reference ground plane (not necessarily the actual ground surface). The positive x coordinate (not shown) is normal to the page, toward the reader. A scatterer is located at position P1 on the reference plane $z = 0$ at ground range dimension y_1. The reference ground plane, in some standard coordinate system, is at a height h_{ref}, so that the actual elevation of the radar is $h = h_{\text{ref}} + H$ and of the scatterer is just h_{ref}. However, h_{ref} is unknown, at least initially. The depression angle of the LOS to P1, relative to the local horizontal, is ψ rad, while the range to P1 is

$$R_0 = \sqrt{y_1^2 + H^2} = \frac{y_1}{\cos\psi} = \frac{H}{\sin\psi}. \tag{6}$$

The radar receiver is coherent; that is, it has both in-phase (I) and quadrature (Q) channels, so that it measures both the amplitude and phase of the echoes. Consequently, the transmitted signal can be modeled as a complex sinusoid [31]:

$$\bar{x}(t) = A\exp[j(2\pi F t + \phi_0)], \qquad 0 \le t \le \tau \tag{7}$$

where F is the radar frequency (RF) in hertz,[3] τ is the pulse length in seconds, A is the real-valued pulse amplitude, and ϕ_0 is the initial phase of the pulse in radians. The overbar on $\bar{x}$ indicates a signal on an RF carrier. The received signal, ignoring noise, is

$$\begin{aligned} &\bar{y}(t) = \hat{A}\rho\exp\left\{ j\left[2\pi F\left(t - \frac{2R_0}{c}\right) + \phi_0\right]\right\}, \\ &\frac{2R_0}{c} \le t \le \frac{2R_0}{c} + \tau. \end{aligned} \tag{8}$$

In (8), ρ is the complex reflectivity of P1 (thus σ, the radar cross section (RCS) of P1, is proportional to $|\rho|^2$) and $\hat{A}$ is a complex-valued constant incorporating the original amplitude A, all radar range equation factors other than σ, and the complex gain of the radar receiver. We assume that ρ is a fixed, deterministic value for now.

After demodulation to remove the carrier and initial phase, the baseband received signal is

$$\begin{aligned} y(t) &= \hat{A}\rho\exp\left(-j\frac{4\pi F R_0}{c}\right) \\ &= \hat{A}\rho\exp\left(-j\frac{4\pi}{\lambda}R_0\right), \qquad \frac{2R_0}{c} \le t \le \frac{2R_0}{c} + \tau. \end{aligned} \tag{9}$$

If this signal is sampled at a time delay t_0 anywhere in the interval $2R/c \le t_0 \le 2R/c + \tau$ (that is, in the range gate or range bin corresponding to range R), the phase

[3] We follow the practice common in digital signal processing literature of denoting unnormalized frequency in hertz by the symbol F, and reserving the symbol f for normalized frequency in cycles, or cycles per sample. A similar convention is used for radian frequencies Ω and ω.

of the measured data sample will be

$$\phi \equiv \arg[y(t_0)] = \arg(\hat{A}) + \arg(\rho) - \frac{4\pi}{\lambda}R_0$$
$$\equiv \phi_{\hat{A}} + \phi_\rho - \frac{4\pi}{\lambda}R_0. \quad (10)$$

Although derived for a simple pulse, this result is not changed in any important way by the use of pulse compression waveforms and matched filters.

Now suppose that P1 is elevated by δh meters to position P2, so that its height is now $h_{\text{ref}} + \delta h$. The range to the scatterer becomes, as a function of the elevation variation δh,

$$R = R(\delta h) = \sqrt{y_1^2 + (H - \delta h)^2}$$
$$= \frac{y_1}{\cos(\psi - \delta\psi)} = \frac{H - \delta h}{\sin(\psi - \delta\psi)}. \quad (11)$$

This increase in height relative to the reference plane reduces the range to the scatterer. This range reduction causes the echo to arrive earlier, and also causes a change in the phase of the demodulated echo sample. We can easily quantify both effects by considering the differential

$$\frac{dR(\delta h)}{d(\delta h)} = \frac{\frac{1}{2}(-2H + 2\delta h)}{\sqrt{y_1^2 + (H - \delta h)^2}} = \frac{\delta h - H}{R(\delta h)} \quad \Rightarrow$$
$$\delta R = -\left[\frac{H - \delta h}{R(\delta h)}\right]\delta h. \quad (12)$$

Evaluating (12) at $\delta h = 0$ gives the effect on the range of a deviation in scatterer height from the reference plane:

$$\delta R = -\left(\frac{H}{R_0}\right)\delta h = -\delta h \sin\psi. \quad (13)$$

The change in echo arrival time will be $2\delta R/c = -2\delta h \sin\psi/c$ seconds. From (10), the received echo phase will change by

$$\delta\phi = -\left(\frac{4\pi}{\lambda}\right)\delta R = \left(\frac{4\pi}{\lambda}\right)\delta h \sin\psi. \quad (14)$$

Equation (14) assumes that the phase of the scatterer reflectivity ρ does not change significantly with the small change $\delta\psi$ in incidence angle of the incoming pulse.

B. Range Foreshortening and Layover

Another effect of the height-induced range change is evident in Fig. 5. Like any radar, a SAR measures range. However, standard SAR signal processing is designed to assume that all echoes originate from a two-dimensional flat surface. Equivalently, the three-dimensional world is projected into a two-dimensional plane.

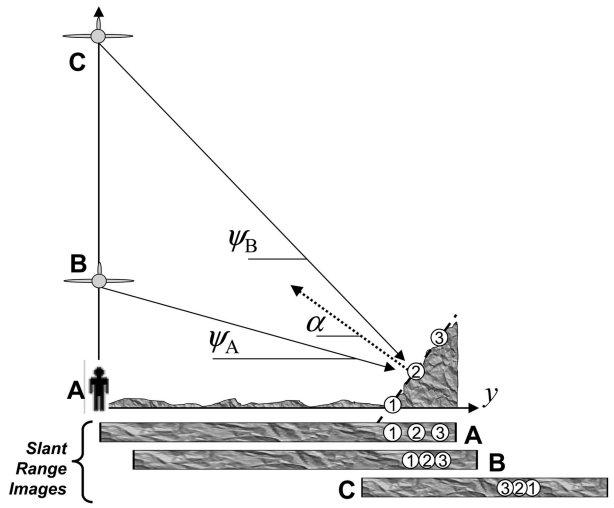

Fig. 6. Layover and foreshortening. Scene viewed from aircraft B is subject to foreshortening. Scene viewed from aircraft C is subject to layover.

Because the radar measures time delay and thus slant range, when the scatterer is at position P2 its echo will be indistinguishable from that of a scatterer located on the ground plane at the range where the planar wavefront[4] impacting P2 also strikes the reference plane. Given an echo of some amplitude at some range R, the SAR processor will represent that scatterer by a pixel of appropriate brightness in the image at a ground range that is consistent with the observed slant range, assuming zero height variation.[5] As shown in Fig. 5, this ground coordinate is

$$y_3 = y_1 - \delta h \tan\psi. \quad (15)$$

Thus, when a scatterer at actual ground range y_1 is elevated by δh meters to position P2, it will be imaged by a standard SAR processor as if it were at location P3.

The imaging of the elevated scatterer at an incorrect range coordinate is termed either layover or foreshortening, depending on the terrain slope and grazing angle and the resultant effect on the image. Fig. 6 illustrates the difference. Three scatterers are shown on sloped terrain. A ground observer and two airborne observers image the scene and project it into the ground plane. The ground observer A observes the true ground ranges of the scene. Airborne observer B measures the scatterers to be at longer ranges due to the platform altitude. Because the grazing angle is below the normal to the terrain slope in the vicinity of scatterers 1, 2, and 3, they are imaged as occurring in the correct order, but with their spacing compressed. This compression of range, while maintaining the

[4]We assume the nominal range is great enough that wavefront curvature can be ignored.

[5]SAR images are naturally formed in the slant plane, but are usually projected into a ground plane for display.

correct ordering of features, is called foreshortening. Airborne observer C images the scene from a higher altitude, with a grazing angle greater than that of the terrain normal. The apparent ranges are longer still, but now the scatterers are imaged in reverse order because scatterer 3 is actually closer to the radar than scatterer 2, and so forth. The term layover refers to this reversal of range. Layover is particularly evident when imaging vertical walls, such as the sides of buildings in urban areas, where the radar is always above the (horizontal) normal to the wall surface.

In sidelooking operation, foreshortening or layover occurs only in the range coordinate. In squinted operation, it occurs in both range and cross-range; details are given in [2], [32]. For simplicity, only sidelooking operation is considered here. Fig. 7 is an image of the U.S. Capitol building where layover is clearly evident in the distorted image of the Capitol dome.

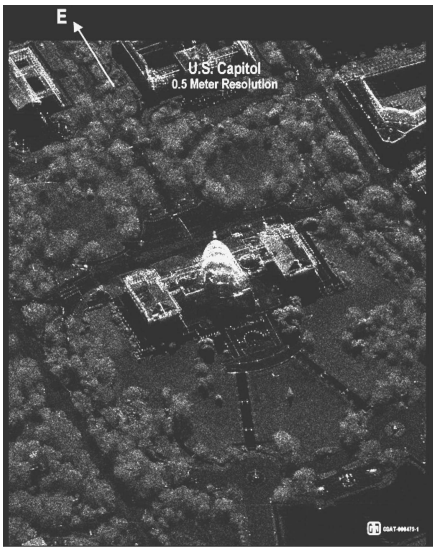

Fig. 7. SAR image of U.S. Capitol building. Distortion of Capitol dome is due in part to layover of dome toward radar, which is imaging the scene from a position above the top of the image. (Image courtesy of Sandia National Laboratories. Used with permission.)

C. The Effect of Height on IFSAR Phase Difference

The output of a SAR image formation algorithm is a complex-valued two-dimensional image: both an amplitude and phase for each pixel. Conventional two-dimensional SAR imaging discards the phase of the final image, displaying only the magnitude information. In IFSAR, the pixel phase data is retained. The echo phase model of (10) can be applied to each pixel of a SAR image $f(x,y)$:

$$\phi_f(x,y) = \phi_{\hat{A}} + \phi_\rho(x,y) - \frac{4\pi}{\lambda} R_f(x,y). \qquad (16)$$

Basic IFSAR uses a sensor having two receive apertures separated by a baseline distance B in a plane normal to the platform velocity vector.[6] The geometry is illustrated in Fig. 8. In this case, the two apertures are located in the y-z plane and separated in the ground range dimension; this might be implemented in practice as two receive antennas (or two subarrays of a phased array antenna) located under the belly of the radar platform. Alternatively, the two apertures could be stacked vertically on the side of the platform, or the baseline could be angled in the y-z plane. All

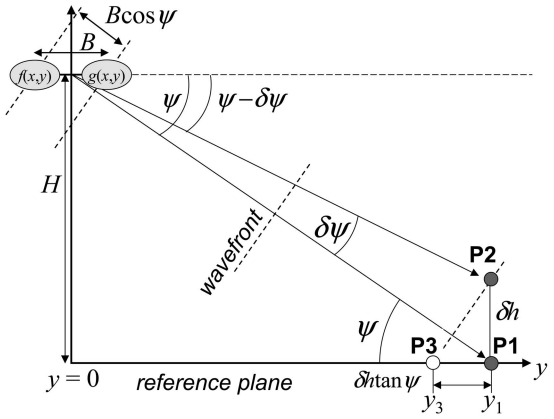

Fig. 8. Geometry for determining effect of scatterer height on IPD.

of these cases produce similar results. For simplicity and conciseness, we consider only the case shown in Fig. 8.

Again consider the two scatterer positions P1 and P2. While various configurations are possible, many one-pass systems transmit from one of the two apertures and receive simultaneously on both, while two-pass systems transmit and receive on the same aperture, but from different positions on the two passes. In the former case, the difference in the two-way radar echo path length observed at the two apertures is ΔR, while in the latter it is $2\Delta R$. This difference results in a factor of two difference in the various interferometric phase difference and height equations. The equations used here are based on a path length difference of $2\Delta R$.

In either case each aperture independently receives the echo data and forms a complex SAR image of the

[6]Interferometry with the baseline orthogonal to the velocity vector is sometimes referred to as cross-track interferometry (CTI), and is used for measuring height variations. Interferometry with the baseline aligned with the velocity vector is referred to as along-track interferometry (ATI), and is used for measuring temporal changes in the SAR scene, e.g. velocity field mapping of waves, glaciers, and so forth. ATI systems typically place two apertures along the side of the platform, one fore and one aft. If the data is obtained by two-pass operation along the same flight path, it is called repeat-pass interferometry (RTI). The focus of this paper is CTI; ATI is not discussed further. RTI is similar to the techniques mentioned in Section IX of this paper. See [1] for a good introduction and comparison of CTI, ATI, and mixed baseline cases.

scene; these images are denoted $f(x,y)$ and $g(x,y)$. The difference in range from P1 to the two aperture phase centers is well approximated as $B\cos\psi$, which is just the projection of the baseline along the LOS. The difference in received phase at the two apertures then becomes, using (16)

$$\phi_{fg}(x,y) \equiv \phi_f(x,y) - \phi_g(x,y) \approx -\frac{4\pi}{\lambda} B\cos\psi. \quad (17)$$

ϕ_{fg} is called the interferometric phase difference (IPD).

Before considering the effect of terrain height variations on the IPD, it is useful to examine the IPD map that results from a perfectly flat scene. Recasting (17) in terms of altitude and ground range, the IPD becomes

$$\begin{aligned}\phi_{fg}(x,y) &\approx -\frac{4\pi}{\lambda} B\cos[\psi(y)] \\ &= -\frac{4\pi B}{\lambda}\left(\frac{y}{R_0}\right) = -\frac{4\pi B y}{\lambda\sqrt{H^2+y^2}} \\ &= -\frac{4\pi B}{\lambda\sqrt{1+(H/y)^2}} \equiv \phi_{fg}^{\mathrm{FE}}(x,y). \end{aligned} \quad (18)$$

Note that this depends on the scatterer's ground range y but not on its cross-range coordinate x, at least for the sidelooking scenarios considered here. This is not surprising as increasing the range to a scatterer clearly increases the received phase shift, but the slightly different geometries to the two receive apertures results in slightly different phase increments, and thus a change in the phase difference. Scatterers at the same range but different cross-ranges present the same geometry and thus the same IPD as the radar platform passes by. The IPD due to scatterers at zero height and a given ground range is called the flat Earth phase difference, here denoted as ϕ_{fg}^{FE}. It is removed during IFSAR processing to form a modified IPD

$$\phi'_{fg} \equiv \phi_{fg} - \phi_{fg}^{\mathrm{FE}}. \quad (19)$$

Once the flat Earth phase ramp has been removed, any additional variations in the IPD will be due to height variations in the scene relative to the flat Earth. Elevating the scatterer at y_1 to height δh will change the depression angle from the center of the IFSAR baseline to the scatterer. The resulting change in ϕ'_{fg} can be found by differentiating (17) with respect to the grazing angle (the (x,y) dependence is dropped temporarily for compactness):

$$\frac{d\phi'_{fg}}{d\psi} = \frac{4\pi}{\lambda} B\sin\psi \quad \Rightarrow \quad \delta\psi = \frac{\lambda}{4\pi B\sin\psi}\delta\phi'_{fg}. \quad (20)$$

This equation states that a change in the IPD of $\delta\phi'_{fg}$ implies a change in depression angle to the scatterer of $\delta\psi$ rad. To relate this depression angle change to an elevation change, consider Fig. 8 again, which shows that

$$\begin{aligned}&\frac{H}{y_1} = \tan\psi \\ &\frac{H-\delta h}{y_1} = \tan(\psi-\delta\psi) \quad \Rightarrow \quad \frac{\delta h}{H} = \frac{\tan\psi - \tan(\psi-\delta\psi)}{\tan\psi}. \end{aligned} \quad (21)$$

Using a series expansion of the tangent function in the numerator and assuming that $\delta\psi$ is small gives

$$\frac{\delta h}{H} \approx \frac{\delta\psi}{\tan\psi} = \delta\psi\cot\psi \quad \Rightarrow \quad \delta h \approx (H\cot\psi)\delta\psi. \quad (22)$$

Finally, using (22) in (20) gives a measure of how much the IPD for a given pixel will change if the scatterer elevation changes [3]:

$$\delta h(x,y) = \frac{\lambda H\cot\psi}{4\pi B\sin\psi}\delta\phi'_{fg}(x,y) \equiv \alpha_{\mathrm{IF}}\delta\phi'_{fg}(x,y) \quad (23)$$

where α_{IF} is the interferometric scale factor. We have reintroduced the (x,y) dependence into the notation to emphasize that this equation applies to each pixel of the SAR maps in IFSAR. Note also that $B\sin\psi$ is the horizontal baseline projected orthogonal to the LOS. Denoting this as $B_\perp$, an alternate expression for the interferometric scale factor is

$$\alpha_{\mathrm{IF}} = \frac{\lambda H\cot\psi}{4\pi B_\perp}. \quad (24)$$

Equation (23) is the basic result of IFSAR.[7] It states that a change in the height of the scatterer relative to the reference plane can be estimated by multiplying the measured change in the interferometric phase difference (after correcting for the flat Earth phase ramp) by a scale factor that depends on the radar wavelength, IFSAR baseline, platform altitude, and depression angle. This result is used in different ways. For conventional IFSAR terrain mapping, it is used to map a difference in IPD from one pixel to the next into an estimate of the change in relative height from the first pixel to the second:

$$h(x_1,y_1) - h(x_2,y_2) \approx \alpha_{\mathrm{IF}}[\phi'_{fg}(x_1,y_1) - \phi'_{fg}(x_2,y_2)]. \quad (25)$$

A height map is formed by picking a reference point (x_0,y_0) in the image and defining the height at that point, $h(x_0,y_0) = h_0$. The remainder of the height map is then estimated according to

$$\hat{h}(x,y) = h_0 + \alpha_{\mathrm{IF}}[\phi'_{fg}(x,y) - \phi'_{fg}(x_0,y_0)]. \quad (26)$$

[7]The sign difference in (23) as compared to [2] arises because the phase at the longer range aperture is subtracted from that at the shorter range aperture in [2], while in this paper the opposite was done.

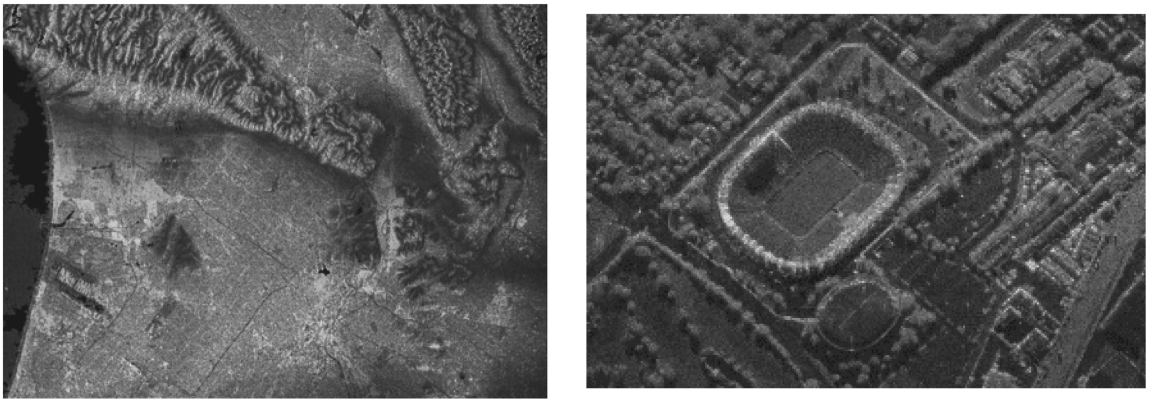

(a) (b)

Fig. 9. Example IFSAR images. (a) Spaceborne image of Los Angeles basin from SRTM data. (b) Airborne image of University of Michigan football stadium and surrounding area. (Image (a) courtesy of NASA/JPL-Caltech. Image (b) courtesy of General Dynamics Advanced Information Systems. Images used with permission.)

If $h_0 = h_{\text{ref}}$, then $\hat{h}$ is the true height h in the coordinate system of interest. However, often one simply chooses $h_0 = 0$, so that $\hat{h}(x,y)$ is a relative height map. Determination of absolute height is addressed in Section VIC.

Equation (23) can also be used to detect changes in scene reflectivity or motion of the terrain itself over time. A discussion of these uses is deferred to Section IX.

As an example of the scale factor between IPD and height, consider the SRTM [33]. The system used one aperture in the cargo bay of the space shuttle, while the other was on the end of a 60 m boom. The shuttle flew at an altitude of about 240 km. The C-band (5.3 GHz, $\lambda = 0.0566$ m) radar operated at a nominal grazing angle of $\psi = 45°$, with the baseline approximately orthogonal to the LOS. With these parameters, $\alpha_{\text{IF}} = 18.02$. Thus a height variation of $\delta h = 1113$ m was sufficient to cause an interferometric phase variation of 2π rad. As another example, consider an X-band (10 GHz, $\lambda = 0.03$ m) airborne system with $H = 5$ km, a horizontal baseline $B = 1$ m, and $\psi = 30°$. The scale factor becomes $\alpha_{\text{IF}} = 41.35$, so that a height change of only 33.8 m corresponds to an interferometric phase variation of 2π rad.

It is useful to confirm our assumption that $\delta\psi$ is small for these two scenarios. Equation (21) is easily rearranged to give

$$\delta\psi = \psi - \arctan\left[\left(1 - \frac{\delta h}{H}\right)\tan\psi\right]. \tag{27}$$

Clearly, if $\delta h \ll H$, the right hand side is nearly zero. For the two specific cases above, (27) shows that a height variation of $\delta h = 100$ m gives a depression angle change of $\delta\psi = 0.5°$ in the airborne case and only $0.012°$ in the spaceborne example, verifying the validity of the small angle assumption.

Equation (23) gives the height variations relative to the reference plane. This plane is the same one to which the platform altitude H is referenced. However, this is not necessarily meaningful in terms of any standard mapping projection. If IFSAR is being performed from a spaceborne platform, then the flat terrain model implicit in Fig. 8 must be replaced by a curved Earth model, complicating the equations; see [1]. Furthermore, the height measured is that from which the radar echoes reflect. This is the Earth surface in bare regions, but may follow the top of the tree canopy in others or, if operating at a frequency or resolution that provides partial penetration of the canopy, some intermediate value.

Fig. 9 gives two examples of IFSAR images, one from a spaceborne system, one from an airborne system. Fig. 9(a) is an image of the Los Angeles area generated from SRTM data. The flat Los Angeles basin is in the center and lower left of the image, while the Santa Monica and Verdugo mountains run along the top of the image. The Pacific coastline is on the left. The two parallel dark strips on the coast are the runways of Los Angeles International airport. Fig. 9(b) is an IFSAR image of the football stadium and surrounding area at the University of Michigan, Ann Arbor. The image shows that the trees above the stadium in the image are taller than those to the left of the stadium, and that the stadium playing surface is actually below the level of the surrounding terrain. (This is much clearer in the color version of the image available on the website mentioned earlier.)

D. Measuring Interferometric Phase Difference

The IPD is easily measured by computing the interferogram

$$\begin{aligned} I_{fg}(x,y) &= f(x,y)g^*(x,y) \\ &= A_f A_g \exp[j(\phi_f - \phi_g)] \end{aligned} \tag{28}$$

so that

$$\arg\{I_{fg}(x,y)\} = (\phi_f - \phi_g) \equiv \phi_{fg}. \quad (29)$$

While the IPD of (29) is the primary function of interest, the amplitude weighting $A_f A_g$ of the full interferogram $I(x,y)$ provides a measure of the SNR of the data and therefore of the quality of the IPD estimate. Note that ϕ_{fg} includes the flat Earth phase ramp ϕ_{fg}^{FE}.

The most important issue in using (23) is the problem of wrapped phase. Because the range to the terrain will be many multiples of the radar wavelength, the phase ϕ_f of (16) will be many radians. In the airborne example above, the nominal one-way range is $5000/\sin(30°) = 10$ km $= 333{,}333.\bar{3}$ wavelengths, so the two-way phase shift is over four million radians. The phase can be expressed as

$$\phi_f = 2\pi k_f + \tilde{\phi}_f \quad (30)$$

for some large integer k_f. $\tilde{\phi}_f$ is the principal value of ϕ_f, which is restricted to the range $(-\pi, +\pi]$. In the above example, $k_f = 666{,}666$ and $\tilde{\phi}_f = 4\pi/3$. The phase that is actually measured by the radar receiver is the wrapped phase

$$\arctan\left(\frac{Q}{I}\right) = \tilde{\phi}_f \quad (31)$$

where I and Q are the in-phase and quadrature channel signal samples. Consequently, (23) computes a height variation of zero for any actual variation that results in a value of $\delta\phi_{fg}$ that is a multiple of 2π. Put another way, unless the phase wrapping can be undone, the height variations will be computed modulo $2\pi\alpha_{\text{IF}}$.

Assume for the moment that, given a wrapped IPD phase function $\tilde{\phi}_{fg}$, it is possible to "unwrap" the phase to recover the original phase value ϕ_{fg}. Only $\tilde{\phi}_f$ and $\tilde{\phi}_g$ can be directly measured. How can we compute $\tilde{\phi}_{fg}$? Consider

$$\begin{aligned}\tilde{\phi}_f - \tilde{\phi}_g &= (\phi_f - 2\pi k_f) - (\phi_g - 2\pi k_g) \\ &= \phi_f - \phi_g + 2\pi(k_g - k_f). \end{aligned} \quad (32)$$

Let $W[]$ be a phase wrapping operator, i.e., $W[\phi] = \tilde{\phi}$. Clearly $W[\phi + 2\pi k] = W[\phi] = \tilde{\phi}$. Then

$$\begin{aligned} W[\tilde{\phi}_f - \tilde{\phi}_g] &= W[\phi_f - \phi_g + 2\pi(k_g - k_f)] \\ &= W[\phi_f - \phi_g] \\ &= \tilde{\phi}_{fg}. \end{aligned} \quad (33)$$

Thus the wrapped IPD can be computed by wrapping the difference between the wrapped phases at the individual apertures. The problem of unwrapping $\tilde{\phi}_{fg}$ to obtain ϕ_{fg} is addressed in Section VIB.

E. Baseline Decorrelation

As discussed after (8), we have assumed that the complex reflectivity ρ of a resolution cell is a constant. For imaging terrain, it is more realistic to model the reflectivity of a resolution cell as the superposition of the echoes from a large number of uncorrelated scatterers randomly dispersed through the resolution cell. The complex reflectivity of a given pixel is therefore modeled as a random variable, typically with a uniform random phase over $[0, 2\pi)$ radians and an amplitude distribution that is strongly dependent on the type of clutter observed [31].[8] The interferogram $I_{fg}(x,y)$ is then also a random process. A common model for the pixel amplitude statistics is a Rayleigh probability density function (pdf).

The complex reflectivity that results from the constructive and destructive interference of scatterers varies with a number of effects, including thermal noise, temporal fluctuations of the clutter (which are used to advantage in Section IX), and observation perspective, including both the differing viewing angles of the two IFSAR apertures and possible rotation of the viewing perspective on different passes. Particularly significant is the effect of the IFSAR baseline, which causes the two apertures to view a given pixel from slightly different grazing angles. If the IFSAR baseline and thus the variation in grazing angle is great enough, the reflectivity of corresponding pixels in the two SAR images will decorrelate. In this event, the IPD will not be a reliable measure of height variations. Zebker and Villasenor derive a simple model for the critical baseline beyond which the images are expected to decorrelate [34]. In terms of grazing angle ψ and the critical baseline length orthogonal to the LOS of the radar, which is the important dimension, the result is

$$B_{c\perp} = \frac{\lambda R}{p \cdot \delta y \tan\psi} \quad (34)$$

where δy is the ground-plane range resolution; note that $\delta y = \delta R \cos\psi$, where δR is the slant range resolution of the radar, and that the result is expressed in terms of range R rather than altitude H. The variable $p = 2$ for systems that transmit and receive separately on each aperture, as in two-pass systems, while $p = 1$ for systems using one aperture to transmit for both receive apertures, typical of one-pass systems.

[8] The RCS σ of the resolution cell, which is proportional to $|\rho|^2$, is thus also a random process. If $|\rho|$ is Rayleigh distributed, then σ has exponential statistics. Pixels having the same mean RCS can thus have varying individual RCS values on any given observation. This random variation of the pixel RCS in areas having a constant mean RCS is called speckle. An introduction to speckle phenomena in IFSAR is available in [6].

The same results expressed as a critical horizontal baseline B_{ch} for consistency with the model used here, and again in terms of a critical vertical baseline B_{cv}, are

$$B_{ch} = \frac{\lambda R \cos\psi}{p \cdot \delta y \sin^2\psi}, \qquad B_{cv} = \frac{\lambda R}{p \cdot \delta y \sin\psi}. \quad (35)$$

Equation (34) shows that steep grazing angles, short ranges, and coarse resolution result in shorter critical baselines, making IFSAR system design more difficult. Continuing the earlier SRTM example with δR = 15 m, p = 1, and assuming that the baseline is approximately orthogonal to the radar LOS gives a critical baseline of $B_{c\perp}$ = 1281 m, far greater than the actual 60 m baseline. Thus, SRTM data collection was not expected to suffer severe baseline decorrelation. As another example, the K_u-band (16.7 GHz, λ = 0.018 m) RTV system [25] uses a vertical baseline and also has p = 1. In its DTED level 4 mode, it uses a range resolution of 0.3 m at a grazing angle of 45°. Assuming a slant range of 10 km, this gives a critical vertical baseline of 849 m, again far greater than the actual baseline of 0.33 m. Another example with a smaller safety margin is repeat-pass IFSAR processing using the SEASAT satellite. This L-band (λ = 0.24 m) system operates from an 800 km orbit altitude with a steep grazing angle of about 67° and a ground range resolution of about 25 m. Applying the horizontal baseline formula with p = 2 estimates the critical baseline at 4532 m. Actual SEASAT baselines formed from orbit pairs viewing the same terrain over a two-week period range from as little as 50 m to 1100 m. Additional analysis and experimental decorrelation data is available in [34].

VI. IFSAR PROCESSING STEPS

Formation of an IFSAR image involves the following major steps:[9]

1) Estimation of the wrapped interferometric phase difference $\tilde{\phi}'_{fg}[l,m]$.
   - formation of the two individual SAR images, $f[l,m]$ and $g[l,m]$;
   - registration of the two images;
   - formation of the interferogram $I_{fg}[l,m]$;
   - local averaging of $I_{fg}[l,m]$ to reduce phase noise;
   - extraction of the wrapped interferometric phase difference $\tilde{\phi}_{fg}[l,m]$ from $I_{fg}[l,m]$;
   - flat Earth phase removal to form $\tilde{\phi}'_{fg}[l,m]$.

2) Two-dimensional phase unwrapping to estimate the unwrapped phase $\phi'_{fg}[l,m]$ from $\tilde{\phi}'_{fg}[l,m]$.

3) Estimation of the terrain map from the unwrapped phase $\phi'_{fg}[l,m]$.
   - baseline estimation;
   - scaling of the unwrapped phase map to obtain the height map $\delta h[l,m]$;
   - orthorectification to develop an accurate three-dimensional map;
   - geocoding to standard coordinates and representations.

Each of these is now discussed in turn.

A. Estimation of the Wrapped Interferometric Phase Difference

The images are formed using any SAR image formation algorithm appropriate to the collection scenario and operational mode, such as the range-Doppler or range-migration (also called ω-k) stripmap SAR algorithms, or polar format spotlight SAR algorithms. Many of the algorithms in common use today are described in [2], [3], [4], [35], [36].

Because the height estimation depends on the difference in phase of the echo from each pixel at the two apertures, it is important to ensure that like pixels are compared. The slightly different geometries of the two offset apertures will result in slight image distortions relative to one another, so an image registration procedure is used to warp one image to align well with the other. Many registration procedures have been developed in the image processing and photogrammetric literature [18]. For one-pass IFSAR, the registration of the two images is usually relatively straightforward given the fixed and well-known geometry of the two apertures, although the baseline attitude and orientation must still be determined precisely. In some one-pass systems, the physical structure is subject to significant flexure, vibration, and oscillation, necessitating the use of laser metrology systems to aid in determining the baseline length and orientation. Examples include the 60 m mast used by SRTM and GeoSAR, which places P-band apertures at the two aircraft wing tips.

Registration is more difficult in two-pass systems, where the baseline can change slightly within the image aperture time and the platform on one pass may be rotated slightly with respect to the other pass, creating mis-registrations that vary significantly across the scene. One registration procedure for these more difficult cases common in IFSAR uses a series of correlations between small subimages of each SAR map to develop a warping function [2, 4]. This concept, called control point mapping or tie point mapping, is illustrated in Fig. 10. The two IFSAR images $f[l,m]$ and $g[l,m]$ are shown in parts (a) and (b) of the figure, respectively. By examining the highlighted subregions carefully, one can see that one image is shifted with respect to the other. Take $f[l,m]$

[9] Use of the indices $[l,m]$ instead of (x,y) indicate that the various maps have been sampled in range and cross-range.

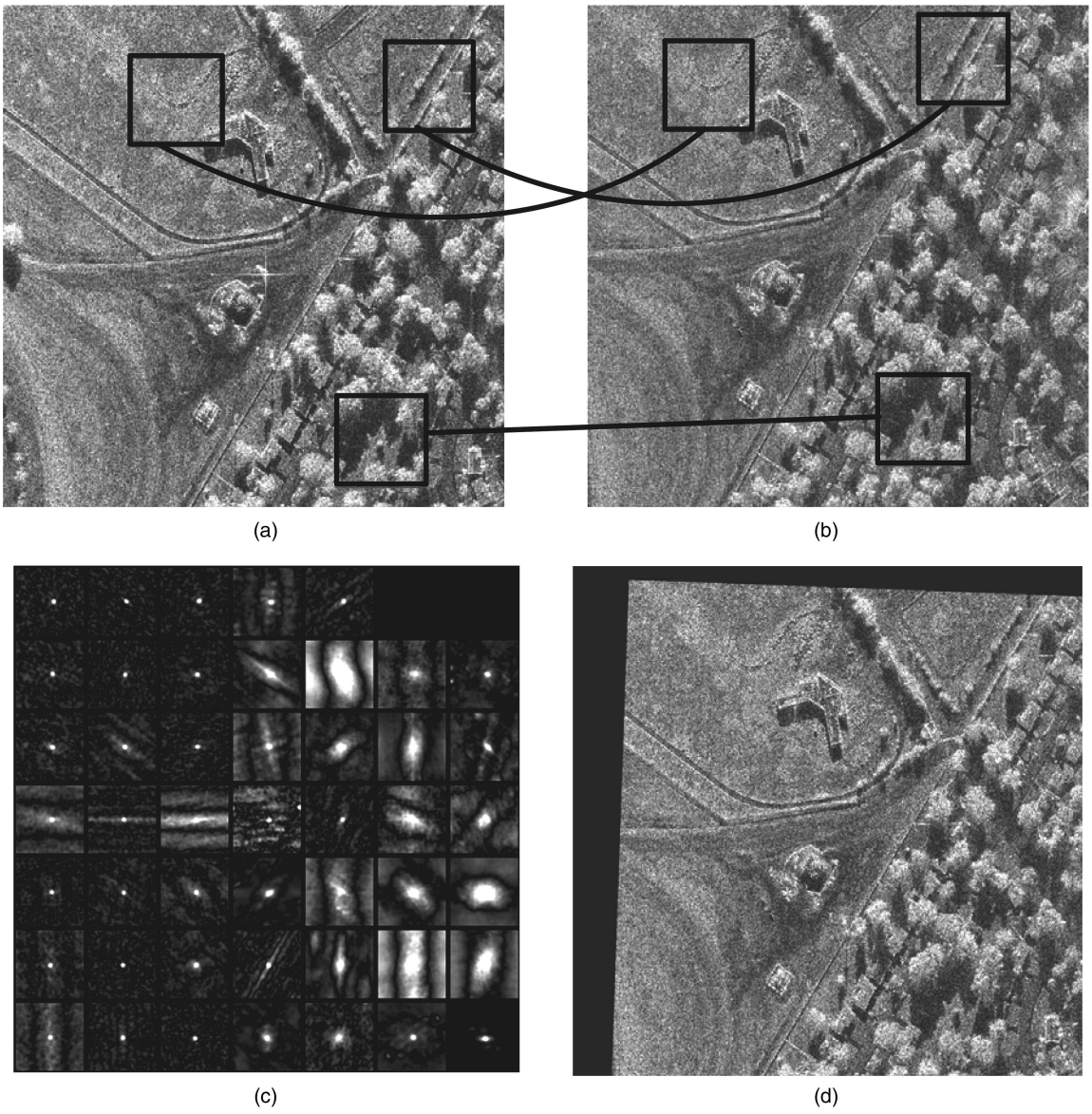

Fig. 10. Illustration of image registration via control point mapping. (a) Master image with three subregions indicated. (b) Secondary image with shift of the highlighted regions visible. (c) 7×7 array of subimage cross-correlation function magnitudes. (d) Secondary image after warping to register with master image. (Images courtesy of Sandia National Laboratories. Used with permission.)

as the "master" image, so that $g[l,m]$ will be warped to align with $f[l,m]$.

The procedure starts by subdividing both images into subimages; in this example, a 7×7 subdivision of the images is considered. A two-dimensional cross-correlation $s_{fg}^{n}[l,m]$ of each of the corresponding pairs of subimages is formed; the superscript n indicates the nth subimage. The magnitude of the 49 resulting correlation functions in shown in Fig. 10(c). Considering just one of these, if a well-defined correlation peak occurs at lag $[0,0]$, it indicates that the two subimages were well aligned in both range and cross-range. If the correlation peak occurs at some non-zero lag $[k_l,k_m]$, it suggests that that region of the secondary image is offset from the corresponding region of the master image by k_l pixels in range and k_m pixels in cross-range.

Registration to within a fraction (typically 1/8 or better) of a pixel is required for good phase unwrapping results; high-fidelity systems may require estimation to within 1/20 of a pixel or better [4, 37]. Consequently, the correlation peak must be located to subpixel accuracy. This can be done by one of several techniques: using oversampled image data, using frequency domain correlation, or using quadratic interpolation of the correlation peak. The latter technique is described in the context of Doppler processing in [31]. The quality of the subimage correlations also varies significantly, as can be seen in Fig. 10(c). If a subregion has low reflectivity, is shadowed, or corresponds to a relatively featureless

terrain such as a body of water, the correlation peak will be diffuse and may be a poor indicator of the required warping. Such subimages can be detected by measuring the peak-to-rms ratio of the subimage correlation:

$$\xi = \frac{\max\{s_{fg}^2[l,m]\}}{\sqrt{\frac{1}{LM}\sum_l \sum_m s_{fg}^2[l,m]}}. \tag{36}$$

ξ will take on higher values for sharp correlation peaks than for diffuse peaks. ξ can then be thresholded to eliminate unreliable subimage correlations.

Once the image warping function required to map the secondary image onto the master image has been estimated, the actual resampling of $g[l,m]$ can be done with any number of interpolation methods. A typical choice that provides adequate quality with relatively low computation is a simple bilinear interpolator, described in detail in [2]. High-fidelity systems may require higher order interpolators for good results.

Numerous additional details and extensions for IFSAR image registration are described in the literature [4, 38]. Some global skews and translations can be corrected in the original data collection and image formation. An iterative approach is often used, with rough registration using correlations of magnitude subimages followed by fine registration using correlation of complex subimages. More recently, registration techniques have been suggested that use subbanding of the image data to estimate registration errors without cross-correlation or interpolation computations. Despite the additional Fourier transforms required, it is claimed that these techniques can achieve registration accuracies of a few hundredths of a resolution cell with reduced computational complexity.

Once the two images are registered, the wrapped phase $\tilde{\phi}_{fg}$ must be computed. As discussed earlier, the clutter within a given resolution cell of one image is typically modeled as a superposition of the echo from many scatterers. The I and Q components that result are zero-mean Gaussian random variables, so that the pixel magnitude is Rayleigh distributed and its phase is uniform. The pdf of the IPD depends on the correlation between the images; the resulting IPD pdf is given in [6]. The maximum likelihood estimator of the wrapped phase map is the phase of an averaged inteferogram [2, 6]:

$$\begin{aligned}\tilde{\phi}_{fg}[l,m] &= \arg\left\{\sum_{n=1}^{N} f[l,m]g^*[l,m]\right\} \\ &= \arg\left\{\sum_{n=1}^{N} I_{fg}[l,m]\right\}.\end{aligned} \tag{37}$$

The N interferogram samples averaged in this equation can be obtained by dividing the SAR data bandwidth into N subbands, forming reduced-resolution images from each, and averaging the interferograms, or by local spatial averaging of a single full-bandwidth interferogram. The latter technique is most commonly used, typically with a 3×3, 5×5, or 7×7 window. The Cramer-Rao lower bound on the variance of the estimated IPD at a particular pixel will be approximately [2]

$$\sigma_{\Delta\phi}^2[l,m] \approx \begin{cases} \dfrac{1}{2N(C/N)^2}, & \text{small } (C/N) \\ \dfrac{1}{N(C/N)}, & \text{large } (C/N) \end{cases} \tag{38}$$

where C/N is the clutter-to-noise ratio at pixel $[l,m]$ and its immediate vicinity. Thus, N-fold averaging reduces the phase variance, and thus the height variance, by the factor N.

Flat-Earth phase removal is often implemented at this point. In this stage, the flat Earth phase function $\phi_{fg}^{\text{FE}}[l,m]$ of (18) is subtracted from $\tilde{\phi}_{fg}$ and the result rewrapped into $(-\pi,\pi]$, giving the wrapped IPD due to terrain variations relative to the flat Earth, $\tilde{\phi}'_{fg}$. Subtracting the flat-Earth interferometric phase reduces the total phase variation, somewhat easing the phase unwrapping step discussed next.

B. Two-Dimensional Phase Unwrapping

The two-dimensional phase unwrapping step to recover $\phi'_{fg}[l,m]$ from $\tilde{\phi}'_{fg}[l,m]$ is the heart of IFSAR processing. Unlike many two-dimensional signal processing operations such as fast Fourier transforms (FFTs), two-dimensional phase unwrapping cannot be decomposed into one-dimensional unwrapping operations on the rows and columns. Two-dimensional phase unwrapping is an active research area; a thorough analysis is given in [39], while [40] provides a good concise introduction.

Before continuing, it is useful to take note of an inherent limitation of phase unwrapping. Adding some multiple of 2π rad to the entire phase map ϕ'_{fg} results in the same value for the wrapped IPD $\tilde{\phi}'_{fg}$. For this reason, even the best phase unwrapping algorithm can only recover the actual IPD to within a multiple of 2π rad. Phase unwrapping can hope to produce good relative height maps, but not absolute height maps. Approaches to finding absolute height are discussed in the Section VIC.

Most traditional phase unwrapping techniques can be classified broadly as either path-following methods or minimum norm methods. Many variants of each general class exist; four algorithms of each type, along with C code to complement them, are given in [39]. A good comparison is presented in [40]. A newer approach based on constrained optimization of network flows is a significant extension of the path-following method [41]. IFSAR phase unwrapping

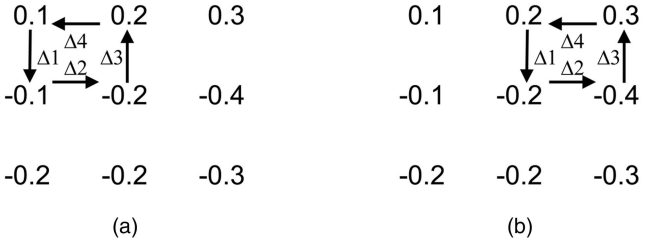

Fig. 11. Illustration of path dependence and residues in two-dimensional phase unwrapping. (a) Path with no residue. (b) Path with residue of -1. See text for details. (After Ghiglia and Pritt [39].)

on real-world data is an extremely difficult problem due to many factors, including for example low SNRs, shadow regions, layover, phase aliasing, and more. These issues, and algorithms to deal with them, are addressed in detail in [39]–[41]. Here, we introduce only the most basic concepts of the major classes of two-dimensional phase unwrapping algorithms.

1) *Path-Following Method*: The path-following approach, which might be better called an integration approach, can be viewed as an extension of one-dimensional phase unwrapping. First, consider a one-dimensional sinusoid of frequency F_0 hertz; the Nyquist sampling rate for this signal is $F_s > 2F_0$. If the sinusoid is sampled at the Nyquist rate or higher, the change in phase from one sample to the next is guaranteed to be less than π rad. Based on this fact, it is well known that an unaliased one-dimensional wrapped phase signal can be uniquely unwrapped (to within an additive multiple of 2π) by simply starting at one end of the signal and integrating (summing) the wrapped phase differences [39].

The path-following approach extends this idea to two dimensions by integrating along an arbitrary path in the two-dimensional discrete $[l,m]$ plane. Clearly, the difference in phase between any two pixels should not depend on the path taken from one to the other. In practice, however, it can and does. The major reasons for such path dependence include pixel-to-pixel phase changes of more than π radians due to aliasing, and phase noise. As a practical matter, aliasing can be very difficult to avoid: large and sudden changes in actual terrain height, say at cliffs or building sides, can cause large changes in the actual IPD.

Path-dependent data can be recognized by a simple test. Consider the idealized 3×3 segment of wrapped phase data in Fig. 11. The values shown are in cycles; thus a value of 0.1 represents a wrapped phase value of 0.2π rad. Because wrapped phases are in the range $(-\pi, +\pi]$, the values in cycles are in the range $(-0.5, +0.5]$. Path dependence can be tested by integrating the wrapped phase difference around a closed path. Because we start and end at the same pixel, the phase values at the beginning and end of the path should be the same. Consequently, the integral of the phase differences around such a path should be zero. In Fig. 11(a), the sum of the differences of the wrapped phase around the path shown is

$$\begin{aligned}\Delta 1 + \Delta 2 + \Delta 3 + \Delta 4 \\ = (-0.2) + (-0.1) + (+0.4) + (-0.1) = 0.\end{aligned} \tag{39}$$

However, the path in Fig. 11(b) has the sum

$$\begin{aligned}\Delta 1 + \Delta 2 + \Delta 3 + \Delta 4 \\ = (-0.4) + (-0.2) + (-0.3) + (-0.1) = -1.\end{aligned} \tag{40}$$

(Note that $\Delta 3 = +0.7$ is outside of the principal value range of $(-0.5, +0.5]$ and therefore wraps to $0.7 - 1.0 = -0.3$.) In this second case, the closed-path summation does not equal zero, indicating an inconsistency in the phase data. A point in the wrapped IPD map where this occurs is called a residue. The particular residue of Fig. 11(b) is said to have a negative charge or polarity; positive residues also occur. Conducting this test for each 2×2 pixel closed path is a simple way to identify all residues in the wrapped IPD map. If residues exist, then the unwrapped phase can depend on the path taken through the data, an undesirable condition.

The solution to the residue problem is to connect residues of opposite polarity by paths called branch cuts, and then prohibit integration paths that cross branch cuts. The allowable integration paths which remain are guaranteed to contain no pixel-to-pixel phase jumps of more than π rad, so that integration will yield consistent unwrapping results.

In a real data set, there may be many residues and many possible ways to connect them with branch cuts. Thus, the selection of branch cuts becomes the major problem in implementing path-following. Indeed, one of the limitations of path-following methods is that portions of the wrapped phase map having high residue densities can become inaccessible, so that no unwrapped phase estimate is generated for these areas and "holes" are left in the unwrapped phase [40]. The most widely-known path-following approach is the Goldstein-Zebker-Werner (GZW) algorithm [42], which is fast and works in many cases. A description of the algorithm is beyond the scope of this article; the reader is referred to [39] and [42] for the details as well as alternative algorithms that can be used when the GZW algorithm fails.

As a very simple, idealized example of the path-following approach, consider the "hill" function shown in Fig. 12. Fig. 13(a) shows the true IPD for this example, while Fig. 13(b) shows the wrapped IPD; this would be the starting point for IFSAR phase unwrapping.[10] Notice the small linear patch of noisy data at about 98.5 m of range. Such a patch could

[10]This example is from simulations of a synthetic aperture sonar system. See [43] for details.

result from low-reflectivity terrain, shadowing, or data corruption. Applying the residue test on each 2×2 pixel loop in this image would reveal a number of residues of polarity either $+1$ or -1 in the vicinity of this noise patch.

Fig. 14 shows the result of unwrapping the phase map of Fig. 13(b) via path-following techniques. Fig. 14(a) is the result obtained with a systematic path that disregards any possible residues. The IPD noise significantly degrades the unwrapped phase. Fig. 14(b) used the GZW algorithm to determine branch cuts, and then unwrapped along a path that avoided branch cut crossings. In this case, the unwrapped phase is indistinguishable from the original IPD before wrapping except at a handful of inaccessible pixels in the noise region.

2) *Least Squares Method*: A second major class of two-dimensional phase unwrapping algorithms are the least squares methods. Whereas the path-following techniques are local in the sense that they determine the unwrapped phase one pixel at a time based on adjacent values, the least squares methods are global in the sense that they minimize an error measure over the entire phase map. A classic example of this approach is the Ghiglia-Romero algorithm described in [44]. This technique finds an unwrapped phase function such that, when rewrapped, it minimizes the mean squared error between the gradient of the rewrapped phase function and the gradient of the original measured wrapped phase. An efficient

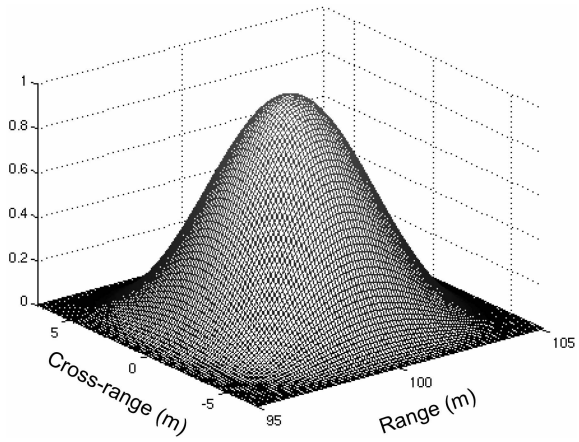

Fig. 12. Artificial "hill" image for demonstrating phase unwrapping performance.

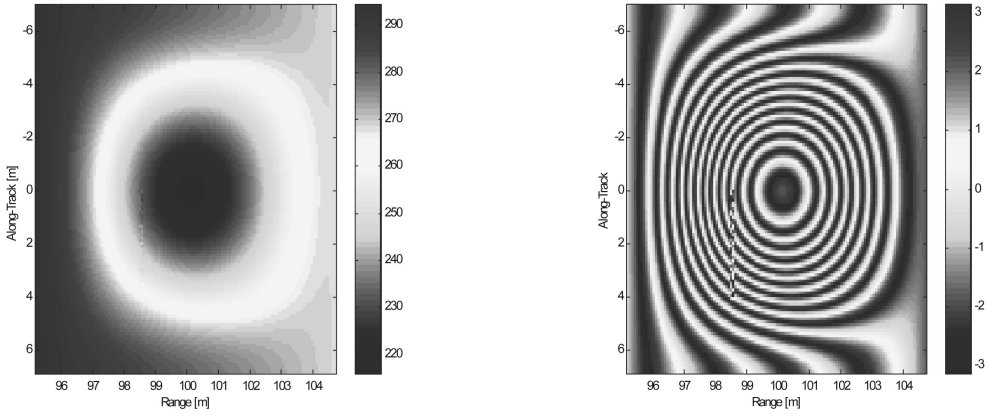

Fig. 13. Interferometric phase data for the "hill" example. (a) Unwrapped. (b) Wrapped.

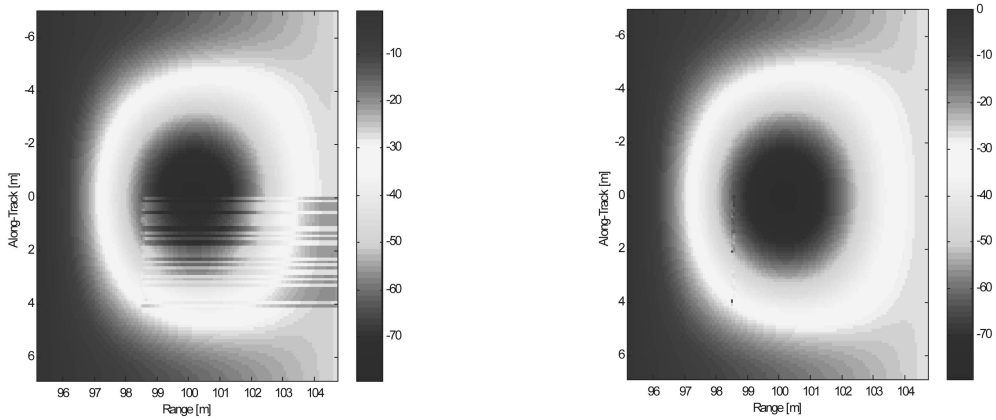

Fig. 14. Phase unwrapping using the path-following technique. (a) Result ignoring residues. (b) Results using GZW algorithm.

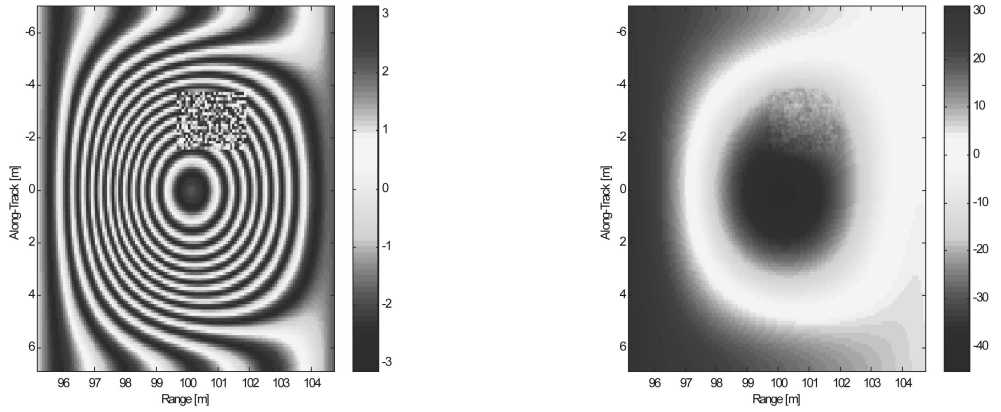

Fig. 15. Phase unwrapping using a minimum norm method. (a) Wrapped phase of "hill" with square noise patch. (b) Unwrapped phase using the unweighted least squares Ghiglia-Pritt algorithm.

algorithm exists to solve this problem using the two-dimensional discrete cosine transform (DCT). The simplest version of the algorithm, called the unweighted least squares algorithm, begins by defining the wrapped gradients of the $M \times N$ raw wrapped IPD data:

$$\Delta_y[l,m] = \begin{cases} W(\tilde{\phi}'_{fg}[l+1,m] - \tilde{\phi}'_{fg}[l,m]), \\ \qquad 0 \le l \le L-2, \quad 0 \le m \le M-1 \\ 0, \qquad \text{otherwise} \end{cases} \tag{41}$$

$$\Delta_x[l,m] = \begin{cases} W(\tilde{\phi}'_{fg}[l,m+1] - \tilde{\phi}'_{fg}[l,m]), \\ \qquad 0 \le l \le L-1, \quad 0 \le m \le M-2 \\ 0, \qquad \text{otherwise.} \end{cases}$$

These are then combined into a "driving function" $d[l,m]$:

$$d[l,m] = (\Delta_y[l,m] - \Delta_y[l-1,m]) + (\Delta_x[l,m] - \Delta_x[l,m-1]). \tag{42}$$

Let $D[k,p]$ be the $M \times N$ two-dimensional DCT_2 of the driving function.[11] The estimate of the unwrapped phase is then obtained as the inverse DCT_2 of a filtered DCT_2 spectrum:

$$\hat{\phi}'_{fg}[l,m] = \mathrm{DCT}_2^{-1}\left\{ \frac{D[k,p]}{2\left\{\cos\left(\frac{\pi k}{M}\right) + \cos\left(\frac{\pi p}{N}\right) - 2\right\}} \right\}. \tag{43}$$

This function is then used in (23) to estimate the terrain height map $\delta h[l,m]$. Note that the DCT-domain filter transfer function is undefined for $k = p = 0$, emphasizing again that the overall phase offset of the estimated map $\hat{\phi}'_{fg}$ is indeterminate.

[11]There are multiple forms of the DCT in common use. The notation "DCT_2" refers to the specific version identified as the "DCT-2" in [45].

Fig. 15(a) is the wrapped phase for the "hill" example of Fig. 12, but with a larger square noise patch added to simulate a low-reflectivity or degraded area. Straightforward application of (41)–(43) produces the unwrapped interferometric phase map estimate of Fig. 15(b). The phase noise remains in the unwrapped map. While it appears to have remained localized, in fact it tends to have a somewhat "regional" influence. This can be seen by comparing Fig. 15(b) to Fig. 14(b), particularly in the "northeast" corner. The general smoothing behavior of minimum norm methods, and their inability to ignore outliers and other corrupted data, means that data errors tend to have a global influence. It can also be shown that they tend to underestimate large-scale phase slopes [40]. On the other hand, they require no branch cut or path computations and consequently produce an unwrapped phase estimate everywhere in the map.

The least squares approach lends itself naturally to an extension that incorporates weights on the data. Generally, the weights are related to an estimate of data quality, so that high-quality data regions have more influence on the solution than low-quality regions. For instance, a weight matrix for the data of Fig. 15 would probably place low or zero weights in the noise region (provided it can be identified), and higher weights elsewhere. The weighted least-squares approach does not lend itself so easily to the use of fast transform techniques. Instead, it is typically formulated as the solution of a set of linear equations, and the equations are solved by one of a number of iterative algorithms. More detailed description of these methods is beyond the scope of this article, but is available in [39].

3) *Network Flow Method*: Constantini [46] described a new approach to phase unwrapping called a network programming or network flow method. This approach represents the gradient of the wrapped IPD map $\tilde{\phi}'_{fg}[l,m]$ as a constrained network with an error in each value that is an integer multiple

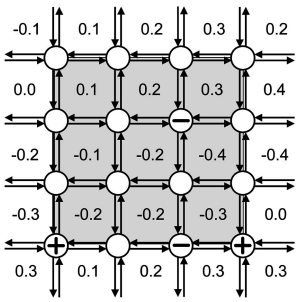

Fig. 16. Network representation of wrapped phase map. Shaded area is same data shown in Fig. 11(b).

of 2π. The unwrapping problem is then posed as a global minimization problem with integer variables. The network structure of the problem allows the application of efficient solution algorithms. The basic approach has been extended and further analyzed, and an excellent description is given in [41].

The network equivalent of the 2D wrapped phase example of Fig. 11(b) is shown in Fig. 16, extended to a larger area. The numbers between the circular nodes are the wrapped phase values, again in cycles. Each node represents the integrated gradient of the four surrounding phase values. Empty nodes represent a zero residue (no phase inconsistency), while "+" and "−" signs inside a node represent residues of $+1$ and -1. The gray shaded area is the portion of the data that was shown in Fig. 11(b). Note that three additional residues occur along the bottom row of nodes in this extended patch of data. The arcs connecting nodes represent the phase gradients from one pixel to the next. The "flow" on an arc is the difference in cycles between the unwrapped and wrapped phase gradient between the two pixels connected by that arc, which must be an integer. To remain consistent with the data, the net flow out of a node must equal the residue at that node. The phase unwrapping problem is now equivalent to finding a set of integers describing the flow on each arc. The solution is not unique. For example, one can simply add one cycle to the flow on each arc of any valid solution to create another valid solution; this corresponds to adding a constant offset of 2π radians to each unwrapped phase value. Thus some optimization criterion is needed to choose one particular solution.

The minimum cost flow (MCF) algorithm solves this problem by minimizing the total number of extra gradient cycles added to the phase map. Efficient algorithms exist for solving the MCF problem in this case. In contrast, typical path-following algorithms seek to minimize the number of places where the wrapped and unwrapped phase gradients disagree, regardless of the amount of the difference. Least squares methods tend to tolerate many small differences while minimizing large differences, thus allowing small unwrapping errors to persist throughout a scene. Another difference is that any errors persisting in the output of the path-following and network programming methods will be multiples of 2π rad, while with least squares methods, errors can take on any value. It is claimed in [41] that the network programming approach with the MCF algorithm provides an effective combination of accuracy and efficiency.

4) *Multi-Baseline IFSAR*: An alternative approach to resolving phase ambiguities utilizes a three phase-center system to provide two different interferometric baselines, and therefore two different ambiguity intervals. This approach is very similar in concept to the multiple-PRI (pulse repetition interval) techniques commonly used to resolve range and Doppler ambiguities in conventional radars [31]. A particular implementation in the RTV system uses two antennas, one a conventional antenna and the other an amplitude monopulse antenna [25]. A baseline of 0.33 m is formed between the conventional antenna and the monopulse sum port, while a second short effective baseline of 0.038 m is formed by the elevation monopulse antenna. The design is such that there are no elevation ambiguities within the elevation beamwidth of the system. This system requires no phase unwrapping algorithm at all; a very simple algorithm suffices to remove the phase ambiguity in the conventional IFSAR image using the monopulse data. The cost of this improvement is that three receiver channels and image formers must be implemented (monopulse sum, monopulse elevation difference, and second antenna). Fig. 17 gives both an orthorectified SAR image of the Pentagon and the corresponding DTED level 4 DEM generated by the RTV system.

C. Estimation of the Terrain Map from the Unwrapped Phase

Equation (23) shows that it is necessary to know the IFSAR baseline precisely to accurately scale the now-unwrapped IPD to height variations. Typical requirements are that the baseline be known to within a factor of 10^{-4} to 10^{-6} of the absolute slant range to the imaged area. The combination of a relatively rigid mechanical baseline structure with modern GPS and inertial navigation system (INS) data will usually allow the baseline length and orientation to be specified accurately enough in one-pass systems, although in systems with flexible baselines laser metrology may also be needed, as commented earlier. However, in two-pass systems, navigational data is often inadequate to estimate the actual baseline to the accuracy required. In this case, there is an extra processing step called baseline estimation necessary to provide the actual baseline length and orientation over the course of the synthetic aperture. A typical approach applies the tie point technique described

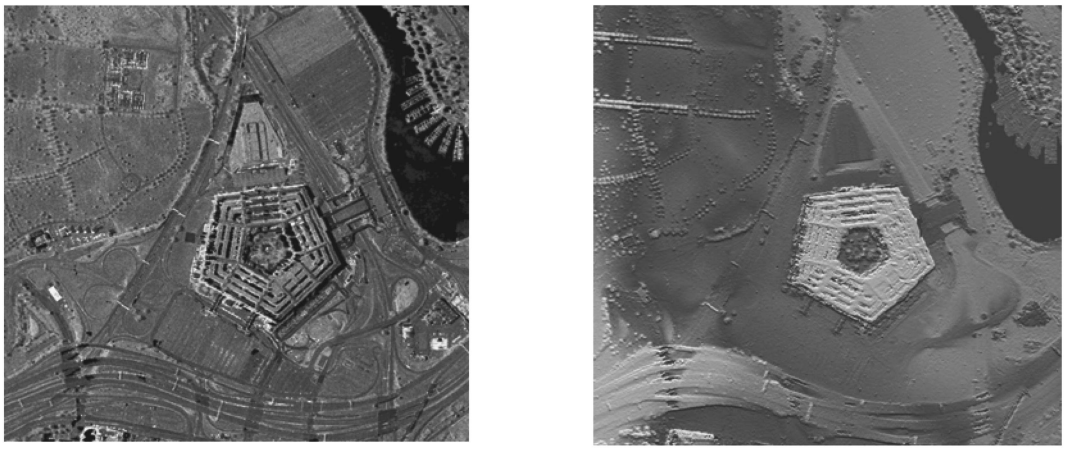

(a) (b)

Fig. 17. DEM of Pentagon generated by RTV system. (a) Orthorectified SAR image, 0.75 m posts. (b) DTED level 4 DEM. (Images courtesy of Sandia National Laboratories. Used with permission.)

above for image registration to estimate the baseline. A technique for least squares estimation of the baseline parameters based on a series of tie point displacements between intensity images is described in [1].

Once the baseline has been estimated, the unwrapped phase map $\hat{\phi}'_{fg}$ is scaled by the interferometric scale factor α_{IF} to get the estimated height profile $\hat{h}(x,y)$ (see (26)). IFSAR processing produces only relative height variations. Absolute height can be estimated by a variety of techniques. The most common is simply the use of one or more surveyed reference points within an image; height relative to this point is then easily converted to absolute height.

An alternative is to attempt to estimate the correct absolute phase shift, and thus absolute height, directly from the radar data. At least two methods have been suggested. The first method splits the fast-time bandwidth in half and completes IFSAR processing separately for each half of the data [47–49]. The effective radar carrier frequency will be different for the two data sets. It can be shown that a differential interferogram formed from the two individual interferograms is equivalent to an interferogram formed using a carrier frequency that is the difference of the two individual half-band frequencies. The individual frequencies can be chosen such that the differential IPD is always in the range $(-\pi,+\pi]$ and is therefore unambiguous. The unwrapped absolute phase can then be estimated from the unwrapped IPD developed earlier, and the differential interferogram phase. Details are given in [47] and [48].

The second method relies on using the unwrapped IPD to estimate delay differences between the two IFSAR channels [49, 37]. However, these differences must be estimated to a precision equivalent to 1% to 0.1% of a pixel in range, requiring very precise interpolation and delay estimation algorithms. In addition, the technique is sensitive to a variety of systematic errors as well as to phase noise. Accuracy is improved by increasing the interpolation ratio (to support finer cross-correlation peak location estimates) and the degree of spatial averaging of the interferogram (to reduce noise). Details are given in [49] and [37].

The next step in IFSAR processing is orthorectification, which uses the newly-gained height information to correct the displacement of image pixels due to layover. For each pixel in the measured (and distorted) SAR image $f[l,m]$, the corresponding height pixel $h[l,m]$ is used to estimate the layover $-h\tan\psi$ (see (15)) present in that pixel, and a corrected image formed by moving the image pixel to the correct location:

$$f'(x,y) = f(x, y + h(x,y)\tan\psi). \tag{44}$$

In general, this will involve fractional shifts of the range coordinate, requiring interpolation of the image in the range dimension. If the radar is operated in a squint mode, there will also be layover in the cross-range (x) dimension, and a similar shift in the x coordinate will be required [2, 32].

The orthorectified image, along with the corresponding height map, locates each pixel in a three-dimensional coordinate system relative to the SAR platform trajectory. To form the final DEM, the data may then translated to a standard geographical coordinate system or projection, a process known as geocoding [4]. The first step is to express the coordinates in the universal Cartesian reference system, which has its origin at the Earth's center, the z axis oriented to the north, and the (x,y) plane in the equatorial plane. The x axis crosses the Greenwich meridian. The next step expresses the heights relative to an Earth ellipsoid, usually the world geodetic system (WGS84) standard ellipsoid.

At this stage, the (x,y,z) coordinates are expressed as a new geographic coordinate set $(\theta_{\text{long}},\theta_{\text{lat}},z)$, where θ_{long} is longitude and θ_{lat} is latitude. The last step projects the geographic coordinates onto a standard cartographic map, such as the universal transverse mercator (UTM), which represents points in a north-east-height (N,E,z) system. Finally, the data is regridded (interpolated) to uniform spacing in the north and east coordinates.

VII. HEIGHT ACCURACY

Since the relative height is estimated as a multiple of the IPD, it is clear that systematic and noise errors in the IPD will translate directly into similar errors in the height estimate. Indeed, one of the advantages of the local smoothing of the IPD performed by the maximum likelihood estimator of (37) is the reduction in phase noise by the factor N in (38). Many IFSAR references present a model for the height error as a function of various geometric and system parameters. Good introductions are given in [50] and [51]. A simple model begins with (1), (2), (4), and (5), repeated here for convenience, which relate scatterer height to system geometry:

$$\begin{aligned}(R+\Delta R)^2 &= R^2+B^2-2BR\cos(\psi+\beta)\\ h &= H-R\sin\psi\\ \Delta R &\approx -B\cos(\psi+\beta)\\ \frac{dh}{d(\Delta R)} &\approx \frac{-R\cos\psi}{B\sin(\psi+\beta)}.\end{aligned} \tag{45}$$

If in addition we model the differential range ΔR in terms of an equivalent measured two-way phase shift $\phi = 4\pi/\lambda$, we obtain an estimate of the sensitivity of height measurements to phase errors:

$$|\delta h| \approx \frac{\lambda R\cos\psi}{4\pi B\sin(\psi+\beta)}|\delta\phi|. \tag{46}$$

Errors in the phase measurements arise from several sources, including thermal noise; various processing artifacts such as quantization noise, point spread response sidelobes, and focusing errors; and decorrelation of echoes between apertures [50]. Decorrelation arises, in turn, from baseline decorrelation, discussed in Section VE, and temporal decorrelation. As has been seen, baseline decorrelation limits the maximum baseline size. Because the interferometric scale factor is inversely proportional to the baseline, a small baseline is preferred for avoiding baseline decorrelation and reducing height ambiguities, while a large baseline is preferred for increased sensitivity to height variations. Temporal decorrelation due to motion of surface scatterers also degrades IFSAR measurements. Decorrelation time scales as observed from spaceborne systems are typically on the order of several days [50].

Phase errors are largely random in nature, and thus tend to increase the variance of the height measurements in a DEM. The specific effect on each individual elevation post measurement varies randomly. The other major sensitivity concern in IFSAR processing is the effect of baseline errors, both length and attitude, on height estimates. This is primarily an issue for two-pass systems. One-pass systems may suffer errors in the knowledge of baseline orientation, but the baseline length is generally accurately known. An approach similar to (45) and (46) can be used to establish the sensitivity of height to baseline length and orientation:

$$\begin{aligned}\frac{dh}{dB} &= \frac{dh}{d(\Delta R)}\cdot\frac{d(\Delta R)}{dB}\\ &\approx \frac{-R\cos\psi}{B\sin(\psi+\beta)}\cdot\{-\cos(\psi+\beta)\} = \frac{R}{B}\frac{\cos\psi}{\tan(\psi+\beta)}\end{aligned} \tag{47}$$

$$\begin{aligned}\frac{dh}{d\beta} &= \frac{dh}{d(\Delta R)}\cdot\frac{d(\Delta R)}{d\beta}\\ &\approx \frac{-R\cos\psi}{B\sin(\psi+\beta)}\cdot B\sin(\psi+\beta) = -R\cos\psi.\end{aligned} \tag{48}$$

Unlike phase-induced errors, height errors due to baseline uncertainties are systematic, affecting each pixel similarly. For instance, an error in estimating the baseline tilt β induces a height shift and a linear tilt of the scene in the cross-track direction. A baseline length error induces a height shift and a quadratic surface distortion. The tilt error can be corrected with two surveyed tie points, the length error with three [51].

Height errors, in addition to being of direct concern, also produce layover errors via (15). Since height errors may contain both systematic and random contributions, so may the layover errors. Layover errors are minimized by minimizing the height errors and by applying tie points.

VIII. SOME NOTABLE IFSAR SYSTEMS

IFSAR has been demonstrated in a variety of spaceborne and airborne systems. While this list is in no way complete, a brief description of a few well-known systems, several of which have already been mentioned, follows. Table II lists approximate values for some of the major parameters of each of these systems. These parameters are considered "approximate" because of limited information regarding the definitions or means of measurement, and inconsistent units and usage among various sources in readily-available literature. The references and web sites cited provide more information about each system.

TABLE II
Approximate Parameters of Some Representative IFSAR Systems

	Airborne Systems				Spaceborne Systems			
	CCRS C-SAR	IFSARE/ STAR-3i	GeoSAR	RTV	RADARSAT 1	SRTM	ERS-1/2 Tandem	ENVISAT ASAR
RF	5.3 GHz	9.6 GHz	353 MHz, 10 GHz	16.7 GHz	5.3 GHz	5.3 GHz, 9.6 GHz	5.3 GHz	5.3 GHz
Altitude	6.4 km	6–12 km	10–12 km	5.5–7 km	798 km	233 km	785 km	780–820 km
1 or 2 pass	1 pass	1 pass	1 pass	1 pass	2 pass	1 pass	2 pass	2 pass
Cross-range Resolution	6–10 m	1.25 m	1–2 m	0.45–1.1 m	8–50 m	30 m	25 m	6–30 m
Post Spacing	2.5–10 m	X: 3 m UHF/P: 5 m	3–10 m	50–200 m	30 m	6–30 m		
Relative Vertical Accuracy	1.5–5 m rms	0.5–1.25 m rms	X: 0.5–1.2 m UHF/P: 1–3 m	1 m LE90	15–50 m rms	X Band: 6 m (90%)	11–14 m rms	
Baseline Length	2.8 m	0.92 m	X: 2.6 m UHF/P: 20 m	0.33 m	60 m	50–500 m	10–500 m	
Baseline Orientation from Horizontal	59°	Horizontal (0°)	Horizontal (0°)	Vertical (90°)	40–70°	30–75°	67°	45–75°
Polarizations	C: HH+HV, VV+VH X: HH	HH	X: VV UHF/P: HH+HV, VV+VH	VV	HH	HH, VV	VV	HH, VV, HH+HV, VV+VH
1st Year of Operation	1991	≈ 1995	2003 (commercial operation)	2001	1995	2000	1995	2002

A. Spaceborne Systems

The Shuttle Radar Topography Mission (SRTM) [27, 28]: The IFSAR system with the greatest public awareness is certainly the space shuttle-based SRTM system. The SRTM refers to the specific 11-day mission flown by the space shuttle Endeavour in February 2000 [27]. The radar was a dual C and X-band IFSAR. One aperture for each band was located in the shuttle cargo bay, while the other was at the end of a 60 m rigid mast extending from the bay. The SRTM mission acquired the data needed to map approximately 80% of the Earth's surface to DTED level 2 specifications in 11 days. Extensive information on the SRTM mission, including imagery and educational materials. can be found at www2.jpl.nasa.gov/srtm/.

"Unedited" C-band data was completed and released to the NGA in January, 2003. In turn, the NGA edited and verified the data, and formatted it into compliance with DTED standards. This task was finished in September 2004. SRTM-derived C-band DTED level 1 and level 2 data is now publicly available through the USGS EROS Data Center at edc.usgs.gov/products/elevation.html. X-band data was processed by the German Aerospace Center (DLR) to DTED level 2 specifications and is available from DLR; more information can be found at www.dlr.de/srtm/level1/start_en.htm.

RADARSAT 1 and 2 [52]: The Canadian Centre for Remote Sensing (CCRS) launched the RADARSAT 1 Earth observation satellite SAR in 1995. RADARSAT 1 is a C-band, single polarization (HH) system. Its primary mission is to monitor environmental change and support resource sustainability. RADARSAT is also a major source of commercially available satellite SAR imagery. Though not initially designed for IFSAR usage, the system is now routinely used in a repeat-pass mode for IFSAR. Orbital and operational considerations result in time between SAR image pairs on the order of days to months. RADARSAT 2, planned for launch in March 2007 at the time of this writing, will extend the data products produced by RADARSAT 1 by adding a capability for full polarimetric scattering matrix (PSM) collection. Information on RADARSAT 1 and 2 is available at www.ccrs.nrcan.gc.ca/radar/index_e.php and at www.radarsat2.info.

ERS-1 and ERS-2 [53–55]: The European Space Agency (ESA) developed the European Remote Sensing (ERS) 1 and 2 satellites SAR systems, launched in 1991 and 1995, respectively. Of special

interest for IFSAR is the ERS 1/2 "tandem mission," in which the satellites fly in the same orbital plane and mean altitude, and with their orbits phased to have the ERS-2 ground track follow that of ERS-1 with a 24 h time lag [53]. This provides the global interferometric coverage of a spaceborne IFSAR with a much shorter temporal baseline than can be supported by RADARSAT, greatly reducing temporal decorrelation. Information on ERS 1 and 2 is available at earth.esa.int/ers/.

ENVISAT [56]: ERS-1/2 were succeeded by ESA's ENVISAT satellite, which carries ten Earth monitoring instruments, among them the advanced SAR (ASAR). Information on the ENVISAT ASAR is available at envisat.esa.int/instruments/asar/.

B. Airborne Systems

CCRS C/X-SAR [57, 58]: The Canadian Centre for Remote Sensing (CCRS) has operated an airborne C-band SAR since 1986; X-band was added in 1988, and a second antenna to support one-pass IFSAR at C-band was added in 1991. The system is mounted on a Convair 580 aircraft. It has been used by the remote sensing research and development community, resource managers, and the exploration, maritime, and mapping industries, as well as to support initial design and marketing for the RADARSAT space-based radar. The CCRS system has been particularly heavily used for along-track interferometry research, especially as applied to mapping ocean currents and glacial movement. Information on the CCRS radar is available at www.ccrs.nrcan.gc.ca/radar/airborne/cxsar/index_e.php.

IFSARE/STAR-3i [59, 60]: Two "IFSAR Elevation" (IFSARE) systems were developed under the sponsorship of the U.S. Advanced Research Projects Agency (ARPA, now DARPA) in 1992–1993 by Norden Systems, Inc. (now part of Northrop Grumman Corp.) and the Environmental Research institute of Michigan (ERIM). The ERIM IFSARE discussed here is now operated by Intermap Technologies, Ltd. and is called the STAR-3i system. The ERIM IFSARE is an X-band system emphasizing relatively rapid generation of digital elevation data for such purposes as site surveys and monitoring for construction and environmental purposes, obtaining elevation data in areas where changes have occurred, tactical military applications, and others. The system is flown on a Learjet. Additional information about the STAR-3i system is available at www.intermap.com.

GeoSAR [61, 62]: GeoSAR is a dual-frequency P- (low UHF) and X-band IFSAR for environmental management and geological, seismic, and environmental hazard identification and monitoring. Developed by the U.S. Jet Propulsion Laboratory, working with Calgis, Inc. and the California Dept. of Conservation, the system is intended to provide both top-of-canopy DSMs with the X-band IFSAR and bald-Earth DEMs using the P-band IFSAR. Similar to the SRTM, a laser ranging system is used to aid in baseline length and orientation estimation. The system is now operated by EarthData, Inc. Additional information on the GeoSAR system is available at www.earthdata.com.

The Rapid Terrain Visualization System [25]: The RTV system was developed by Sandia National Laboratories for the U.S. Army with the purpose of "rapid generation of digital topographic data to support emerging crisis or contingencies." The RTV is a K_u-band system flown on a deHavilland DHC-7 aircraft. The system has at least two unique aspects. The first is the use of an elevation monopulse antenna for one of the apertures to enable multi-baseline IFSAR processing, eliminating the need for explicit phase unwrapping. The second is real-time on-board generation of mosaiced IFSAR data products at peak area mapping rates of 10 km^2/min (DTED level 3) or 3.5 km^2/min (DTED level 4). Additional information is available at www.sandia.gov/radar/rtv.html.

IX. OTHER APPLICATIONS OF IFSAR

The IPD between two SAR images can be used in other ways. IFSAR presumes that there is no change in the imaged scene between the two image data collections, so phase differences are due only to height variations viewed from slightly different aspect angles. This assumption is clearly true in one-pass systems, but may not be in two-pass systems, a problem referred to as temporal decorrelation. As mentioned earlier, the time between passes in two-pass satellite systems might be on the order of hours, but also might be weeks. This "problem" can also be an opportunity: IFSAR can be used to detect changes in terrain height over significant time periods.

Terrain motion mapping examines the change in phase due to a change in scatterer height at a fixed location on the ground between two different times [2]. As with IFSAR static terrain mapping, we again assume that the reflectivity $\rho(x,y)$ of each pixel does not change between images. Because only a single receive aperture is used, (14) can be applied directly to estimate the change in height at each pixel between imaging passes:

$$\widehat{\delta h}(x,y) = h(x,y;t_1) - h(x,y;t_0) \approx \frac{\lambda}{4\pi \sin\psi}[\phi(x,y;t_1) - \phi(x,y;t_0)]. \quad (49)$$

This equation assumes that the terrain motion between passes is in the vertical dimension only. In fact, in many cases, such as earthquakes or glacial flows, the motion is primarily horizontal. Any change

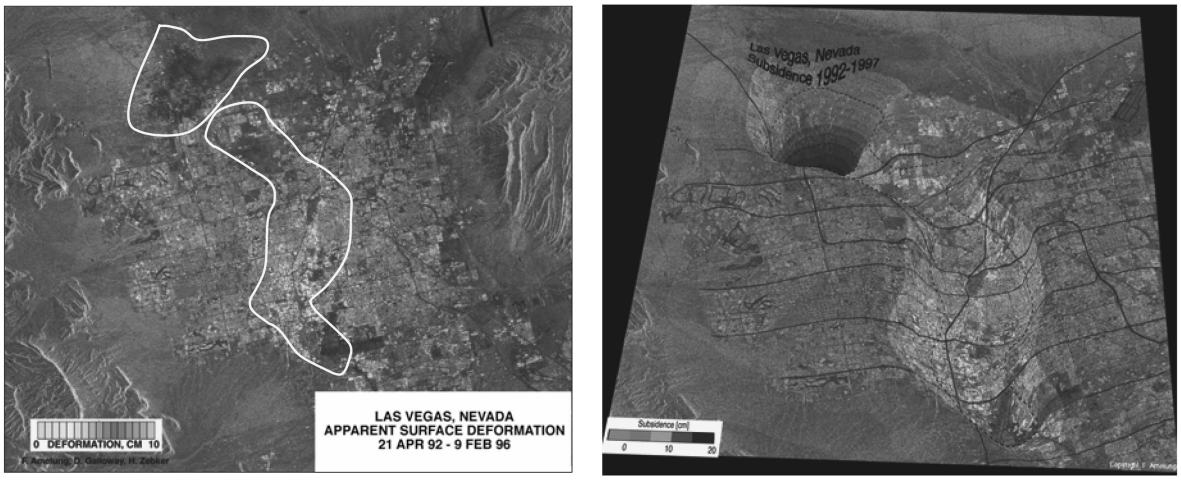

(a) (b)

Fig. 18. IFSAR-based terrain motion map showing land subsidence in Las Vegas, NV over a nearly 4 yr period. (a) IFSAR-based terrain motion map. Subsidence is significant primarily in the outlined regions, with the subsidence being greatest in the darker region in the upper left quadrant. (b) Three-dimensional visualization of subsidence effects. (Images courtesy of the Radar Interferometry Group, Stanford University. Used with permission.)

in slant range between a scatterer and the radar will result in a detectable change in the IPD, and suitable generalizations of (49) can be developed for horizontal motion of the terrain.

Clearly, terrain motion mapping requires two-pass operation. The time interval could be on the order of days or weeks to study the effects of such phenomena as earthquakes or volcanic explosions, or it could be years to study phenomena such as glacier movement or ground subsidence. The processing operations are essentially the same as discussed earlier.

Fig. 18 is an example of using terrain motion mapping to monitor land subsidence. The map is of the Las Vegas, NV area and covers a nearly 4 yr time period. Fig. 18(a) is the IFSAR terrain motion map; outlines have been added to indicate the areas of greatest subsidence. These are more easily viewed in the color version available on the web site cited earlier. Fig. 18(b) is a dramatic three-dimensional visualization generated from this data. Notice the sensitivity of the technique: the subsidence is ones of centimeters over 4 years! The subsidence in this case is due to inelastic compaction of the aquifer [63].

Ideally, exactly the same flight path would be followed on the two passes, so that the baseline between the two images is zero. In practice, this is very difficult, and a small non-zero baseline will be reflected in the data. This means the IPD will have components due to both the temporal change in height, and the static height profile. One approach to removing the static component is to use an existing DEM to estimate it and then subtract its contribution to the phase [2].

Another application of growing interest is coherent change detection (CCD) [2]. Like terrain motion mapping, CCD is a two-pass application that compares two images taken from the same trajectory at different times. The time intervals are typically shorter, from a few minutes apart to many hours or days apart. However, we now assume the terrain height profile is unchanged, but the reflectivity function $\rho(x,y)$ does change. This could occur due to disturbance of the ground by persons or vehicles, but also due to wind blowing tree leaves and other natural phenomena. In general, both the amplitude $|\rho|$ and phase ϕ_ρ will change. If there is no change in the reflectivity of a given pixel between passes, computing a normalized correlation coefficient of the two measurements $\rho_1(x,y)$ and $\rho_2(x,y)$ should produce a value approximately equal to 1.0. If the reflectivity has changed, a lesser value of the correlation coefficient should result.

It is shown in [2] that the maximum likelihood estimate of the change in reflectivity is given by

$$\alpha = \frac{2\left|\sum_k f_0^* f_1\right|}{\sum_k |f_0|^2 + \sum_k |f_1|^2} \tag{50}$$

where f_0 and f_1 represent the two images taken at times t_0 and t_1, and it is understood that the equation is applied to each pixel of the images to form a two-dimensional correlation map. The summation over k indicates averaging over a local two-dimensional window, similar to (37). Typical windows range from 3×3 to 9×9. Values of α near 1.0 indicate an unchanged reflectivity between passes; values near 0.0 indicate a changed reflectivity. However, (50) can be misleading if there is any mismatch in the power of the two images. Another estimator that is robust to average power differences uses the geometric mean in

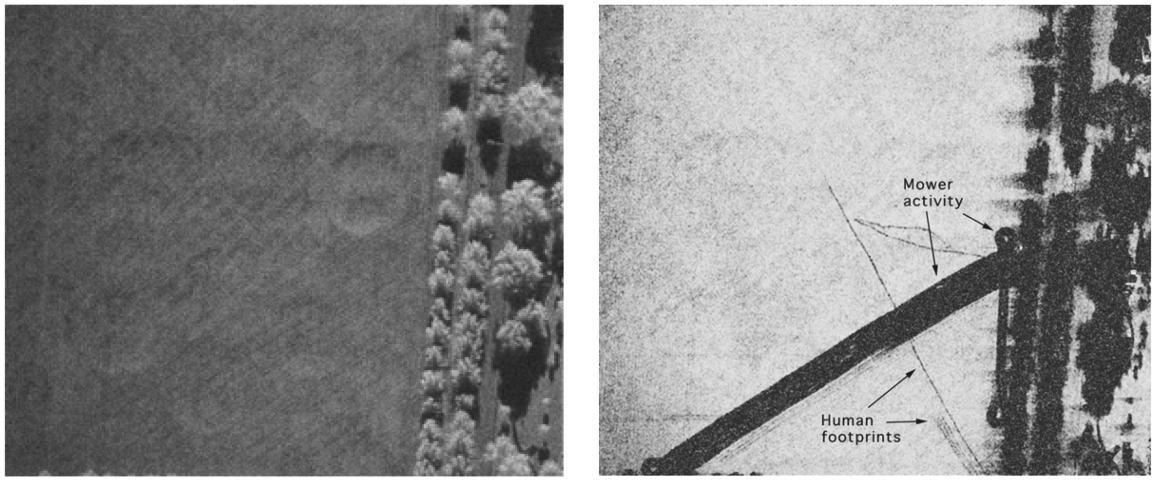

(a) (b)

Fig. 19. IFSAR-based CCD. (a) One of a pair of SAR images of a field bordered by trees. (b) CCD change map showing mower activity and footprints of pedestrians. The trees decorrelate due to leaf motion. (Images courtesy of Sandia National Laboratories. Used with permission.)

the denominator:

$$\alpha = \frac{\left|\sum_k f_0^* f_1\right|}{\sqrt{\left(\sum_k |f_0|^2\right)\left(\sum_k |f_1|^2\right)}}. \tag{51}$$

A CCD map can provide a very sensitive indicator of activity in an observed area. Fig. 19(a) shows one of a pair of SAR images of a field bordered by a stand of trees; the second image would appear identical to the eye. The data for the two images was collected on flight passes separated by approximately 20 min. Fig. 19(b) is the CCD change map formed from the image pair. Light-colored pixels represent values of α near 1.0, while dark pixels represent values near 0.0. The map clearly shows a broad diagonal dark streak and another vertical, narrower streak where mowers had cut the field, changing its reflectivity, between the two SAR passes. Also visible are some narrow trails where pedestrians walked in the scene, disturbing the field surface. Note that the trees also decorrelated between passes. This is due to wind blowing the individual leaves that comprise the composite response of each pixel, effectively randomizing the pixel reflectivity phase ϕ_ρ between passes.

REFERENCES

[1] Madsen, S. N., and Zebker, H. A.
Imaging radar interferometry.
Principles & Applications of Imaging Radar (Manual of Remote Sensing (3rd ed.), vol. 2), New York: Wiley, 1998.

[2] Jakowatz, C. V., Jr., et al.
Spotlight Mode Synthetic Aperture Radar.
Boston: Kluwer Academic Publishers, 1996.

[3] Carrara, W. G., Goodman, R. S., and Majewski, R. M.
Spotlight Synthetic Aperture Radar.
Norwood, MA: Artech House, 1995.

[4] Franceschetti, G., and Lanari, R.
Synthetic Aperture Radar Processing.
New York: CRC Press, 1999.

[5] Rosen, P. A., Hensley, S., Joughin, I. R., Li, F. K., Madsen, S. N., Rodriguez, E., and Goldstein, R. M.
Synthetic aperture radar interferometry.
Proceedings of IEEE, **88**, 3 (Mar. 2000), 333–381.

[6] Bamler, R., and Hartl, P.
Synthetic aperture radar interferometry.
Inverse Problems, **14** (1998), R1–R54.

[7] Gens, R., and Vangenderen, J. L.
SAR interferometry—Issues, techniques, applications.
International Journal of Remote Sensing, **17**, 10 (1996), 1803–1835.

[8] Massonnet, D., and Feigl, K. L.
Radar interferometry and its application to changes in the earth's surface.
Review of Geophysics, **36**, 4 (Nov. 1998), 441–500.

[9] Rogers, A. E. E., and Ingalls, R. P.
Venus: Mapping the surface reflectivity by radar interferometry.
Science, **165** (1969), 797–799.

[10] Zisk, S. H.
A new Earth-based radar technique for the measurement of lunar topography.
Moon, **4** (1972), 296–300.

[11] Graham, L. C.
Synthetic interferometric radar for topographic mapping.
Proceedings of IEEE, **62** (June 1974), 763–768.

[12] Zebker, H. A., and Goldstein, R. M.
Topographic mapping from interferometric SAR observations.
Journal of Geophysical Research, **91** (1986), 4993–4999.

[13] Goldstein, R. M., Zebker, H. A., and Werner, C. L.
Satellite radar interferometry: Two-dimensional phase unwrapping.
Radio Science, **23**, 4 (July/Aug. 1988), 713–720.

[14] Li, F., and Goldstein, R. M.
Studies of multibaseline spaceborne interferometric synthetic aperture radars.
IEEE Transactions on Geoscience and Remote Sensing, **28** (1990), 88–97.

[15] Richman, D.
Three dimensional, azimuth-correcting mapping radar.
U.S. patent 4,321,601, Mar. 23, 1982.

[16] Gamba, P., and Houshmand, B.
Digital surface models and building extraction: A comparison of IFSAR and LIDAR data.
IEEE Transactions on Geoscience and Remote Sensing, **38**, 4 (July 2000), 1959–1968.

[17] Mercer, B.
Combining LIDAR and IfSAR: What can you expect?
Proceedings Photogrammetric Week 2001, 227–237 (Institute for Photogrammetry, University of Stuttgart). Available at www.intermaptechnologies.com or www.ifp.uni-stuttgart.de/publications/phowo01/phowo01.en.htm.

[18] Leberl, F. W.
Radargrammetric Image Processing.
Norwood, MA: Artech House, 1990.

[19] Mercer, B.
DEMs created from airborne IFSAR—An update.
Presented at the International Society for Photogrammetry and Remote Sensing, Commission II, ISPRS XXth Congress, Istanbul, Turkey, July 12–23, 2004.
Published in the *International Archives of Photogrammetry, Remote Sensing and Spatial Information Science*, XXXV-B2, 841–848.

[20] Weibel, R., and Heller, M.
A framework for digital terrain modeling.
In *Proceedings of the 4th International Symposium on Spatial Data Handling*, vol. 1, Zurich, Switzerland, July 1990, 219–229.

[21] United States Geological Survey (USGS)
U.S. GeoData Digital Elevation Models Fact Sheet.
Available at erg.usgs.gov/isb/pubs/factsheets/fs04000.html.

[22] Intermap Technologies Corporation
www.intermap.com.

[23] Melvin, W. L., Showman, G. A., and Guerci, J. R.
A knowledge-aided GMTI detection architecture.
In *Proceedings of 2004 IEEE Radar Conference*, Philadelphia, PA, Apr. 26–29, 2004.

[24] U.S. National Geospatial-Intelligence Agency
Performance Specification, Digital Terrain Elevation Data (DTED).
MIL-PRF-89020B, May 23, 2000.

[25] Burns, B. L., Eichel, P. H., Hensley, W. H., and Kim, T. J.
IFSAR for the rapid terrain visualization demonstration.
In *Conference Record of Asilomar Conference on Signals, Systems, and Computers*, vol. 1, Pacific Grove, CA, Oct. 2000, 8–15.

[26] Roth, M. W.
High-resolution interferometric synthetic aperture radar for Discoverer II.
Johns Hopkins APL Technical Digest, **20**, 3 (1999), 297–304.

[27] Rabus, B. et al.
The shuttle radar topography mission—A new class of digital elevation models acquired by spaceborne radar.
ISPRS Journal of Photogrammetry and Remote Sensing, **57** (2003), 241–262.

[28] Shuttle Radar Topography Mission (SRTM)
Jet Propulsion Laboratory, National Aeronautics and Space Administration.
http://www2.jpl.nasa.gov/srtm/.

[29] Mercer, J. B.
SAR technologies for topographic mapping.
In D. Fritsch and D. Hobbie, (Eds.), *Photogrammetric Week 1995*, Stuttgart, Germany, 117–126.

[30] Goldstein, R.
Atmospheric limitations to repeat-track radar interferometry.
Geophysical Research Letters, **22**, 18 (1995), 2517–2520.

[31] Richards, M. A.
Fundamentals of Radar Signal Processing.
New York: McGraw-Hill, 2005.

[32] Sullivan, R. J.
Microwave Radar: Imaging and Advanced Concepts.
Norwood, MA: Artech House, 2000.

[33] Hensley, S., Rosen, P., and Gurrola, E.
The SRTM topographic mapping processor.
In *Proceedings IEEE 2000 International Geoscience and Remote Sensing Symposium* (IGARSS '00), vol. 3, July 2000, 1168–1170.

[34] Zebker, H. A., and Villasenor, J.
Decorrelation in interferometric radar echoes.
IEEE Transactions on Geoscience and Remote Sensing, **30**, 5 (Sept. 1992), 950–959.

[35] Curlander, J. C., and McDonough, R. N.
Synthetic Aperture Radar: Systems and Signal Processing.
New York: Wiley, 1991.

[36] Cumming, I. G., and Wong, F. H.
Digital Processing of Synthetic Aperture Radar Data.
Norwood, MA: Artech House, 2005.

[37] Imel, D. A.
Accuracy of the residual-delay absolute-phase algorithm.
IEEE Transactions on Geoscience and Remote Sensing, **36**, 1 (Jan. 1998), 322–324.

[38] Scheiber, R., and Moreira, A.
Coregistration of interferometric SAR images using spectral diversity.
IEEE Transactions on Geoscience and Remote Sensing, **38**, 5 (Sept. 2000), 2179–2191.

[39] Ghiglia, D. C., and Pritt, M. D.
Two-Dimensional Phase Unwrapping: Theory, Algorithms, and Software.
New York: Wiley, 1998.

[40] Zebker, H. A., and Lu, Y.
Phase unwrapping algorithms for radar interferometry: Residue-cut, least-squares, and synthesis algorithms.
Journal of the Optical Society of America, **15**, 3 (Mar. 1998), 586–598.

[41] Chen, C. W., and Zebker, H. A.
Network approaches to two-dimensional phase unwrapping: Intractability and two new algorithms.
Journal of the Optical Society of America, **17**, 3 (Mar. 2000), 401–414.

[42] Goldstein, R. M., Zebker, H. A., and Werner, C. L.
Satellite radar interferometry: two-dimensional phase unwrapping.
Radio Science, **23**, 4 (1989), 3268–3270.

[43] Bonifant, W. W., Jr., Richards, M. A., and McClellan, J. H.
Interferometric height estimation of the seafloor via synthetic aperture sonar in the presence of motion errors.
IEE Proceedings—Radar, Sonar, and Navigation, **147**, 6 (Dec. 2000), 322–330.

[44] Ghiglia, D. C., and Romero, L. A.
Robust two-dimensional weighted and unweighted phase unwrapping that uses fast transforms and iterative methods.
Journal of the Optical Society of America, **11**, 1 (Jan. 1994), 107–117.

[45] Oppenheim, A. V., and Schafer, R. W.
Discrete-Time Signal Processing (2nd ed.) (with J. R. Buck).
Upper Saddle River, NJ: Prentice-Hall, 1999, sect. 8.8.2.

[46] Constantini, M.
A novel phase unwrapping method based on network programming.
IEEE Transactions on Geoscience and Remote Sensing, **36**, 3 (May 1999), 813–821.

[47] Madsen, S. N., and Zebker, H. A.
Automated absolute phase retrieval in across-track interferometry.
In *Proceedings of IEEE 1992 Geoscience and Remote Sensing Symposium* (IGARSS '92), vol. 2, 1992, 1582–1584.

[48] Madsen, S. N., Zebker, H. A., and Martin, J.
Topographic mapping using radar interferometry: Processing techniques.
IEEE Transactions on Geoscience and Remote Sensing, **31** (Jan. 1993), 246–256.

[49] Madsen, S. N.
On absolute phase determination techniques in SAR interferometry.
In *Proceedings of SPIE*, Algorithms for Synthetic Aperture Radar Imagery II, vol. 2487, Orlando, FL, Apr. 19–21, 1995, 393–401.

[50] Zebker, H. A., et al.
Accuracy of topographic maps derived from ERS-1 interferometric radar.
IEEE Transactions on Geoscience and Remote Sensing, **32**, 4 (July 1994), 823–836.

[51] Rodriguez, E., and Martin, J. M.
Theory and design of interferometric synthetic aperture radars.
IEE Proceedings—F, **139**, 2 (Apr. 1992), 147–159.

[52] Geudtner, D., et al.
RADARSAT repeat-pass SAR interferometry.
In *Proceedings IEEE 1998 International Geoscience and Remote Sensing Symposium* (IGARSS '98), vol. 3, July, 6–10 1998, 1635–1637.

[53] Duchossois, G., and Martin, P.
ERS-1 and ERS-2 tandem operations.
European Space Agency *ESA Bulletin*, 83 (1995), 54–60.

[54] Rufino, G., Moccia, A., and Esposito, S.
DEM generation by means of ERS tandem data.
IEEE Transactions on Geoscience and Remote Sensing, **36**, 6 (Nov. 1998), 1905–1912.

[55] Shiping, S.
DEM generation using ERS-1/2 interferometric SAR data.
In *Proceedings of IEEE 2000 Geoscience and Remote Sensing Symposium* (IGARSS 2000), vol. 2, 2000, 788–790.

[56] Suchail, J.-L., et al.
The ENVISAT-1 advanced synthetic aperture radar instrument.
In *Proceedings of IEEE 1999 Geoscience and Remote Sensing Symposium* (IGARSS 1999), vol. 2, 1999, 1441–1443.

[57] Gray, A. L., Mattar, K. E., and Farris-Manning, P. J.
Airborne SAR interferometry for terrain elevation.
In *Proceedings IEEE 1992 International Geoscience and Remote Sensing Symposium* (IGARSS '92), vol. 2, 1992, 1589–1591.

[57] Gray, A. L., Mattar, K. E., and Farris-Manning, P. J.
Airborne SAR interferometry for terrain elevation.
In *Proceedings IEEE 1992 International Geoscience and Remote Sensing Symposium* (IGARSS '92), vol. 2, 1992, 1589–1591.

[58] Livingstone, C. E., et al.
The Canadian Airborne R&D SAR Facility: The CCRS C/X SAR.
In *Proceedings IEEE 1996 International Geoscience and Remote Sensing Symposium* (IGARSS '96), vol. 3, May 27–31, 1996, 1621–1623.

[59] Adams, G. F., et al.
The ERIM interferometric SAR: IFSARE.
IEEE *AES Systems Magazine*, (Dec. 1996), 31–35.

[60] Mercer, J. B., Thornton, S., and Tennant, K.
Operational DEM production from airborne interferometry and from RADARSAT stereo technologies.
In *Proceedings 1998 American Society for Photogrammetry and Remote Sensing–Resource Technology, Inc. Conference* (ASPRS-RTI), Tampa, FL, Mar. 31–Apr. 3, 1998

[61] Wheeler, K., and Hensley, S.
The GeoSAR airborne mapping system.
In *Record of IEEE 2000 International Radar Conference*, 2000, 831–835.

[62] Hensley, S., et al.
First P-band results using the GeoSAR mapping system.
In *Proceedings IEEE 2001 Geoscience and Remote Sensing Symposium* (IGARSS 2001), vol. 1, 2001, 126–128.

[63] Amelung, F., et al.
Sensing the ups and downs of Las Vegas: InSAR reveals structural control of land subsidence and aquifer-system deformation.
Geology, **27**, 6 (June 1999), 483–486.

Mark A. Richards (S'72—M'82—SM'86) is a principal research engineer and adjunct professor in the School of Electrical & Computer Engineering at the Georgia Institute of Technology. He has 25 years experience in academia, industry, and government in radar signal processing and embedded computing, and is the author of *Fundamentals of Radar Signal Processing* (McGraw-Hill, 2005). He has served as a program manager in the Defense Advanced Research Projects Agency; the general chair of the IEEE 2001 Radar Conference, and as an associate editor of the *IEEE Transactions on Image Processing* and the *IEEE Transactions on Signal Processing*. Dr. Richards teaches frequently in graduate and professional education courses in radar signal processing, radar imaging, and related topics.